ARTICLES
https://doi.org/10.1038/s41588-021-00782-6
nature genetics

Check for updates

Base-resolution models of transcription-factor binding reveal soft motif syntax

Žiga Avsec[1,2,7], Melanie Weilert[3], Avanti Shrikumar[4], Sabrina Krueger[3], Amr Alexandari[4], Khyati Dalal[3,5], Robin Fropf[3], Charles McAnany[3], Julien Gagneur[1], Anshul Kundaje[4,6] ✉ and Julia Zeitlinger[3,5] ✉

The arrangement (syntax) of transcription factor (TF) binding motifs is an important part of the cis-regulatory code, yet remains elusive. We introduce a deep learning model, BPNet, that uses DNA sequence to predict base-resolution chromatin immunoprecipitation (ChIP)–nexus binding profiles of pluripotency TFs. We develop interpretation tools to learn predictive motif representations and identify soft syntax rules for cooperative TF binding interactions. Strikingly, Nanog preferentially binds with helical periodicity, and TFs often cooperate in a directional manner, which we validate using clustered regularly interspaced short palindromic repeat (CRISPR)-induced point mutations. Our model represents a powerful general approach to uncover the motifs and syntax of cis-regulatory sequences in genomics data.

Understanding the cis-regulatory code of the genome is vital for understanding when and where genes are expressed and how genetic variation and somatic mutations affect disease. Despite extensive efforts to map millions of putative enhancers in a wide variety of cell types and tissues[1–3], identification of the critical bases that alter their regulatory information remains a major challenge. It is known that short sequence motifs are critical for the binding of sequence-specific TFs, but how motif combinations and their syntactic arrangements influence TF binding in vivo is not well understood. For example, two or more strictly spaced motifs may form composite motifs that provide a platform for DNA-mediated cooperativity between the corresponding TFs[4]. However, whether less strict (soft) motif spacing preferences exist within enhancers and influence TF cooperativity is not clear. The precise rules of the cis-regulatory code remain to be elucidated.

Experimental manipulations of enhancer sequences, such as mutations or synthetic designs, strongly support the existence of motif syntax[5–12]. However, genome-wide analyses have rarely identified statistically over-represented motif syntax rules, questioning whether they exist and impose evolutionarily constraints on enhancer function[13–17]. One limitation is that motif instances are typically identified as over-represented sequences matching position weight matrix (PWM) models[18–21]. When patterns are discovered computationally[22–28], they are difficult to validate experimentally and the mechanism by which they might affect TF cooperativity is not clear. For example, over-represented instances of strict motif spacings are sometimes associated with retrotransposons that contain multiple TF-binding motifs[23,24]. On the other hand, when experimental TF binding data are available—that is, from ChIP experiments coupled to sequencing (ChIP–seq)[29–34], inference of motif syntax is still limited by the low resolution of putative binding events identified using peak-callers[29–34].

There is hence a critical need for a general method that can identify cis-regulatory motif syntax based on genome-wide experimental data. Convolutional neural networks (CNNs) have recently been applied to accurately predict diverse molecular phenotypes, including TF binding from DNA sequence[35–38]. The advantage of CNNs is that they can learn flexible predictive models composed of hierarchical layers of arbitrarily complex, nonlinear pattern detectors, to capture de novo sequence motifs and their higher-order organizational context without making strong biological assumptions. However, the complexity of these models makes them particularly challenging to interpret. While several methods have been developed to visualize TF-binding motifs from trained CNNs[35,36,38–42], methods for extracting the rules by which motif syntax informs TF binding are lacking[43].

Another critical limitation is the resolution of current CNN models. State-of-the-art models of TF binding predict binary binding events[35–37] or low-resolution continuous binding signal averaged across windows of 100–200 base pairs (bp)[44]. This can limit the ability to learn motif syntax that promotes TF cooperativity[43], which probably exists in ChIP–seq experiments. For example, TFs sometimes bind indirectly to motifs of other TFs[16,24,45–47]. TF cooperativity is even more apparent when the resolution of ChIP–seq is improved by the addition of an exonuclease digestion step (ChIP–exo)[48]. ChIP–exo methods such as ChIP–nexus generate base-resolution footprints precisely over the motif instances bound by the TF in vivo[49,50], and these footprints differ between motifs bound directly and indirectly[50,51]. ChIP–nexus profiles have also provided evidence that TFs may help the binding of another TF nearby[52]. Although the full extent of TF cooperativity at the level of binding is not known, these results indicate that ChIP–seq data, and especially ChIP–nexus data, are a useful readout for cis-regulatory motif syntax if the data are modeled at sufficiently high resolution.

To discover motif syntax, we developed a new CNN called BPNet that models the relationship between cis-regulatory sequence and TF binding profiles at base resolution. We studied the pluripotency TFs Oct4, Sox2, Nanog and Klf4 in the well-characterized mouse

[1]Department of Informatics, Technical University of Munich, Garching, Germany. [2]Graduate School of Quantitative Biosciences, Ludwig-Maximilians-Universität München, Munich, Germany. [3]Stowers Institute for Medical Research, Kansas City, MO, USA. [4]Department of Computer Science, Stanford University, Stanford, CA, USA. [5]The University of Kansas Medical Center, Kansas City, KS, USA. [6]Department of Genetics, Stanford University, Stanford, CA, USA. [7]Present address: DeepMind, London, UK. ✉e-mail: akundaje@stanford.edu; jbz@stowers.org

embryonic stem cell (ESC) model, generating ChIP–nexus data for maximum resolution. We trained base-resolution BPNet models on these ChIP–nexus profiles with high predictive performance, on par with concordance between replicate experiments. We extended model interpretation methods to extract new motif representations that are not based on statistical over-representation but directly summarize the predictive influence on TF binding. We then developed methods that use the trained BPNet model as an in silico oracle to measure how the distance between motif pairs affects TF cooperativity. We find that strict motif spacings in the genome are mainly due to retrotransposons, but that TF cooperativity depends on preferential soft motif syntax that is in agreement with experimentally characterized protein–protein or nucleosome interactions in ESCs. We also observe unexpected rules of TF binding cooperativity, including a broad preference for Nanog to bind DNA with helical periodicity, and perform experimental validations.

These results suggest that end-to-end neural network models trained on high-resolution genomics data, coupled with a dedicated suite of interpretation tools, can serve as a powerful tool for discovery of the critical bases within cis-regulatory sequences and identification of the underlying motif syntax associated with TF cooperativity.

Results

BPNet predicts TF binding profiles from sequence. We performed ChIP–nexus experiments for Oct4, Sox2, Nanog and Klf4 in mouse ESCs and obtained genome-wide, strand-specific base-resolution profiles for each TF (Fig. 1a). As shown for previous TF ChIP–nexus data[49], the profiles at known TF-binding motifs show consistent stereotypical footprints across various genomic regions, as illustrated by the binding of Oct4 and Sox2 to the composite *Oct4–Sox2* motif[53] (Fig. 1b). These footprints not only had higher resolution compared to ChIP–seq data, but also displayed increased motif specificity. For example, the *Sox2* motif showed a sharp ChIP–nexus footprint for Sox2 but not for Oct4, while ChIP–seq data showed binding signal for both (Fig. 1c). We identified 147,974 genomic regions of 1-kb length exhibiting statistically significant and reproducible enrichment of ChIP–nexus signal for Oct4, Sox2, Nanog or Klf4.

In contrast to all current deep learning models for TF binding, we designed BPNet to provide direct prediction of the raw base-resolution binding profiles from DNA sequence. Binding profiles can be decomposed into the total signal (read counts) and the profile shape (base-resolution distribution of reads). We reasoned that the profile shape should be predictable from 1-kb genomic sequences, since minimal enhancer activity can typically be reproduced outside its genomic context with sequences of <500 bases[54,55]. The total signal, however, could be influenced by factors that are not modeled, including chromatin state and higher-order chromatin organization.

To achieve high prediction accuracy, BPNet was designed with the following properties (Fig. 1d). (1) BPNet is a CNN that uses filters of 25-bp width in the first convolutional layer to scan the 1-kb region for relevant sequence motifs, followed by nine dilated convolutional layers with residual skip connections[56,57] and exponential dilation in every layer[44,58] to learn increasingly complex predictive sequence patterns with a 1-kb receptive field. To preserve base resolution, pooling is not used. (2) BPNet uses multitask learning to jointly train on the strand-specific ChIP–nexus profiles of all four TFs. (3) Experimental control data are used as an auxiliary input (protein-attached chromatin capture (PATCH–CAP) for ChIP–nexus data[59]). The signal from this track is regressed out during training, which prevents BPNet from learning these experimental biases. (4) BPNet uses a multiscale loss function for separate evaluation of the predictions of profile shape (using a multinomial negative log-likelihood loss) and total read counts (using a mean-squared error loss). Model training, hyperparameter tuning and performance evaluation were performed on different sets of genomic regions in distinct chromosomes.

To evaluate predictive performance, we inspected individual enhancers located on held-out test chromosomes such as those associated with the genes *Lefty1* (ref. [60]), *Zfp281* (ref. [61]) and *Sall1* (refs. [62,63]) and found that the predicted and observed ChIP–nexus profiles were noticeably similar, with highly concordant summits of footprints (Fig. 1e and Extended Data Fig. 1a). We then systematically compared the positions of high ChIP–nexus counts between predicted versus observed profiles in all regions of the held-out test set. Strikingly, the positional concordance at resolutions ranging 1–10 bp was on par with replicate experiments and substantially better than randomized profiles, average profiles and the control track (PATCH–CAP) (Fig. 1f). Other measures of profile concordance confirmed the high prediction performance (Extended Data Fig. 1b). We also confirmed that the mappability of regions did not bias the predictions (Supplementary Fig. 1). These results show that BPNet accurately learned to predict the ChIP–nexus binding profiles of all four TFs from DNA sequence.

To identify key components for the high-prediction performance, we systematically varied the network architecture (Fig. 1g and Extended Data Fig. 1c–e). We found that the large number of convolutional layers was critical for prediction of all four ChIP–nexus datasets and was particularly important for Nanog (Fig. 1g). This indicates that the learned sequence patterns required to predict ChIP–nexus profiles span over larger sequence regions beyond individual motifs[64], especially in the case of Nanog. We also found that the relative priority of the profile versus total count prediction tasks during training affected prediction performance. Up-weighting the profile prediction task improved the performance of profile predictions. However, irrespective of relative task weight, the model's performance for total count prediction ($R_s = 0.62$) did not match replicate concordance ($R_s = 0.94$; Extended Data Fig. 1f). These results are consistent with our assumption that longer sequences or other measurements, such as local chromatin state, may be required for optimal prediction of total TF occupancy[64], but that local sequence context (1 kb) is sufficient for accurate prediction of the shape of ChIP–nexus profiles.

A suite of model interpretation tools for TF-binding motifs. We next set out to extract the sequence features that were predictive of TF binding from the trained BPNet model. We extended our previously developed tool DeepLIFT[65] to quantify the contribution of each base within an input sequence to the entire predicted ChIP–nexus profile of each TF (Fig. 2a; Methods). These TF-specific contribution scores are illustrated at the distal *Oct4* enhancer, where all four TFs show strong predicted footprints matching the observed ChIP–nexus footprints (Fig. 2b (top) and Supplementary Fig. 2a).

Subsequences with high contribution scores, which we call seqlets, often resemble TF-binding motifs (Fig. 2b, middle). One prominent seqlet matches the composite *Oct4–Sox2* motif, which has previously been mapped to this exact position in the *Oct4* enhancer[66]. This motif has high contribution scores for Oct4 and Sox2, which are directly bound to the motif, and slightly lower scores for Nanog and Klf4 (Fig. 2b, middle), indicating that the *Oct4–Sox2* motif could be indirectly important for the binding of other TFs.

Other seqlets did not readily match known motifs. For example, we found a TGAT sequence in the middle of the Nanog footprint (highlighted in Fig. 2a, middle), but it was unclear whether this is a *Nanog* motif since previous reports on its consensus are conflicting[47,67–72]. These results demonstrate the ability of contribution scores to highlight TF-binding motifs, but also indicate the need to identify and characterize the motifs more systematically.

Next, we used TF–Modisco[41] to systematically discover and summarize recurring predictive sequence patterns into consolidated

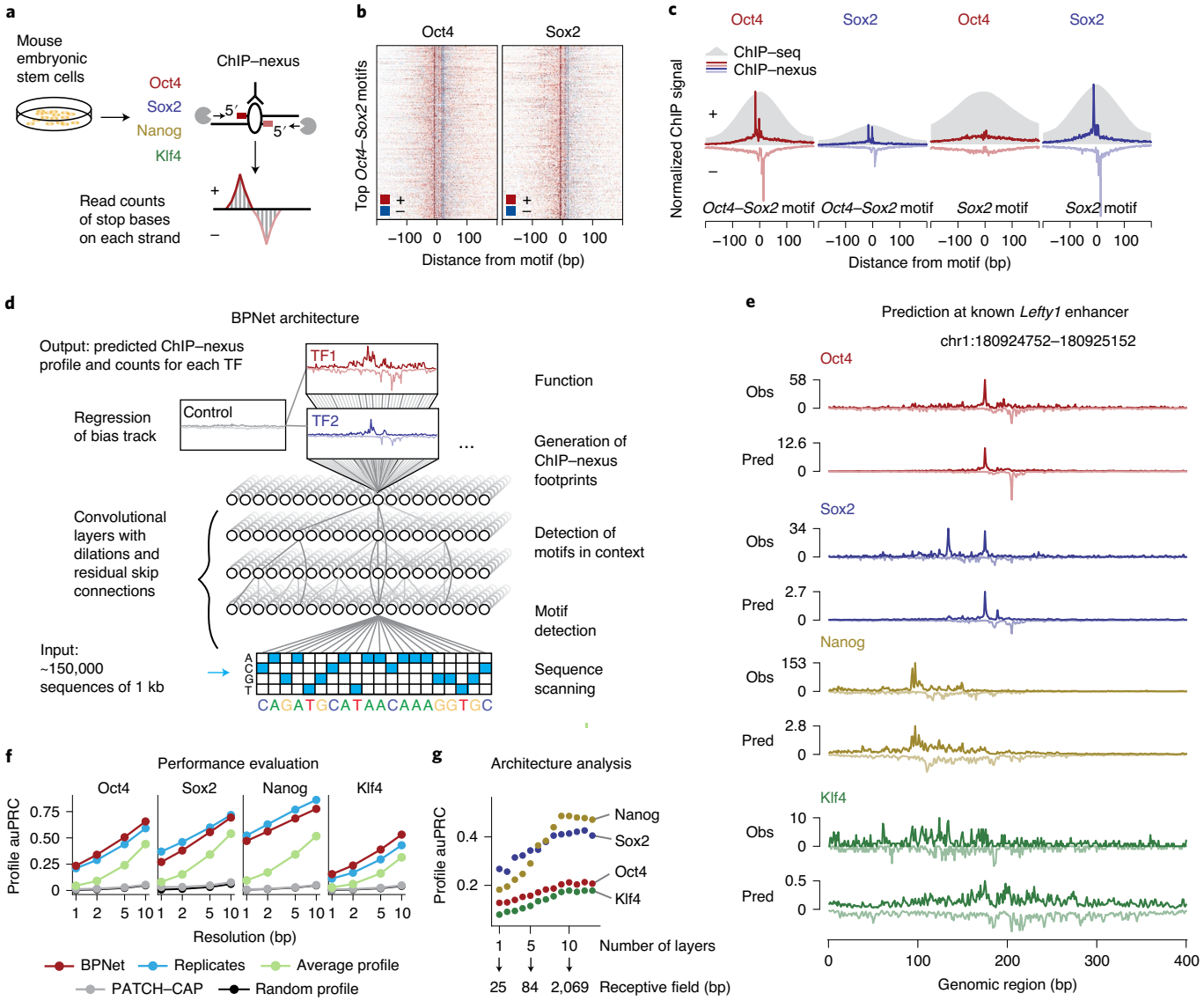

Fig. 1 | BPNet predicts ChIP-nexus signal at base resolution. a, ChIP-nexus experiments were performed on Oct4, Sox2, Nanog and Klf4 in mouse ESCs. After digestion of the 5′ DNA ends with lambda exonuclease, strand-specific stop sites were mapped to the genome at base resolution. Bound sites exhibit a distinct footprint of aligned reads, where the positive (+) strand peak occurs many bases before the negative (–) strand peak. **b**, Profile heatmaps of Oct4 and Sox2 ChIP-nexus data at the 500 *Oct4-Sox2* motifs with the most ChIP-nexus reads (color depth for each strand represents normalized signal intensity). **c**, Average Oct4 and Sox2 ChIP-nexus footprints and ChIP-seq profiles at the 500 *Oct4-Sox2* or *Sox2* motifs with the most reads. The ChIP-nexus data have higher resolution and show less unspecific binding of Oct4 to the *Sox2* motif. **d**, Architecture of the convolutional neural network (BPNet) that was trained to simultaneously predict ChIP-nexus read counts at each strand for all TFs from 1-kb DNA sequences, while being prevented from learning information already explained by a bias track (PATCH-CAP control). **e**, Observed (Obs) and predicted (Pred) ChIP-nexus read counts for the *Lefty* enhancer located on held-out test chromosome 8. **f**, BPNet predicts the positions of high ChIP-nexus signal within the profiles at replicate-level accuracy as measured by area under the precision-recall curve (auPRC) at resolutions from 1 to 10 bp in held-out test chromosomes 1, 8 and 9. Results for the average ChIP-nexus profile, PATCH-CAP control profile and a randomized profile are shown as control. **g**, More convolutional layers (*x* axis) increase the number of input bases considered for profile prediction at each position (receptive field), and this yields increasingly more accurate profile shape predictions on the tuning chromosomes 2–4 (measured in auPRC as above), showing that larger sequence context is important.

motifs from the sequences of all bound regions and their associated base-resolution contribution scores. For each TF, TF–Modisco uses contribution scores to identify, align and cluster seqlets across all bound sequences into consolidated motifs (Fig. 2c). For each cluster, a new motif representation called contribution weight matrix (CWM) is derived by averaging the contribution scores of each of the four possible bases at every position across the seqlets. A more traditional position frequency matrix (PFM) representation, which contains the normalized base frequencies rather than the average contribution scores, is also calculated (the Supplementary Note gives further details on CWMs and PFMs/PWMs).

TF–Modisco discovered 51 motifs, but 18 of these had unusually long PFMs (>40 bp) with high information content (30–100 bits) (Fig. 2d and Extended Data Fig. 2a). This implies that the genomic instances of these motifs share near identical base composition across the entire length of the pattern (despite being discovered by using only uniquely mappable ChIP–nexus reads). Indeed, we found that the majority of them (>80%) overlapped with annotated repeat elements

(Extended Data Fig. 2b). The most common were long-terminal repeats of endogenous retrotransposon viruses (ERVs), including those of the ERVK, ERVL and the ERVL-MaLR family (Extended Data Fig. 2c). Remarkably, the corresponding CWM representations of these long PFMs were quite different. Rather than long stretches of uniformly over-represented bases, the CWMs highlighted the shorter subsequences predictive of TF binding (Fig. 2d and Extended Data Fig. 2c). This difference between CWM and PFM representations provides a means to discover and pinpoint bound motifs within retrotransposons.

The remaining 33 motifs were all interpretable TF-binding motifs but contained subsets with subtle differences, leading us to select 11 representative motifs for further analysis (Extended Data Fig. 2d and Supplementary Fig. 3). These motifs include the well-known *Oct4–Sox2*, *Sox2* and *Klf4* motifs, as well as the *Zic3* and *Esrrb* motifs, which bind pluripotency TFs that we did not profile. All motifs were overall robustly discovered by TF–Modisco from five different BPNet models trained on different subsets of ChIP–nexus peak regions (Supplementary Fig. 4).

Using the 11 representative motifs, we then comprehensively mapped and labeled all predictive motif instances in the bound genomic regions. We scanned the base-resolution contribution scores of all regions and annotated predictive motif instances that had high contribution scores and high match scores to the CWM (Fig. 2c). In total, we obtained 241,005 unique motif instances in the 147,974 genomic regions, with *Klf4* motifs occurring most frequently (Fig. 2e). Altogether, 72,696 regions (48.1%) have at least three motif instances while 20,352 (13.5%) have at least five (Fig. 2f). These genome-wide motif annotations are in agreement with motif instances supported by previous independent validation experiments[73–75] (Supplementary Fig. 2b–d) and provide a strong foundation for analysis of genome-wide motif syntax and the characterization of known functional enhancers in mouse ESCs (Fig. 2b, bottom and Supplementary Fig. 5).

The motif maps derived from BPNet outperformed those obtained by traditional approaches such as PWM scanning, assessed by ChIP–nexus footprint height (Extended Data Fig. 3 and Supplementary Note). BPNet correctly identified more motif instances supported by footprints in sequences from held-out test chromosomes than either MEME[18–21] or HOMER[76], especially for the short *Nanog* motif. The improved performance was achieved because PWM-based motif scanning methods compute match scores using only sequence similarity while the BPNet method also incorporates predictive contribution scores derived from the entire 1-kb sequence (Supplementary Fig. 6). The higher motif accuracy requires training of BPNet on base-resolution profiles rather than coarse-resolution binary (bound versus unbound) labels (Supplementary Note and Extended Data Fig. 4). This suggests that BPNet leverages the profiles to learn the importance of motif instances in their larger sequence context, thereby reducing the false discovery rate.

Our method also outperformed traditional methods when using an independent, previously published, assay for transposase -accessible chromatin (ATAC)-seq dataset[77] for evaluation. After induced depletion of Oct4 or Sox2, regions with differential chromatin accessibility (as defined by the authors) overlapped more *Oct4–Sox2* and *Sox2* motif instances ranked by BPNet contribution scores than those ranked by motif scores from either MEME or HOMER (Fig. 2g and Supplementary Fig. 7a). These results support the high accuracy of BPNet-mapped motif instances relative to those obtained from traditional motif discovery and scanning methods. They also confirm the link between the in vivo binding of Oct4 and Sox2 and their effect on chromatin accessibility.

Finally, we found that the quantitative changes in ATAC-seq signal following Oct4 and Sox2 depletion can also be accurately predicted from BPNet TF binding models. Specifically, linear models trained using the sequence features encoded in the final convolutional layer of the BPNet model were able to accurately predict differential accessibility (Fig. 2h). These models outperformed linear models trained using only the inferred motif instances (Supplementary Fig. 7b). Our results indicate that the complete sequence representation learned by BPNet encodes predictive features beyond the linear, additive effects of the motif instances. Hence, we set out to identify higher-order sequence features such as motif syntax.

Composite motifs and indirect binding footprints. As a first step towards identifying motif syntax, we inspected the motifs identified by TF–Modisco for composite motifs, the simplest form of motif syntax. Indeed, we discovered not only the *Sox2* motif and the monomeric *Oct4* motif[78], but also the composite *Oct4–Oct4* motif (Fig. 3a), a near-palindromic motif that resembles the MORE and PORE motifs bound by Oct4 homodimers[79,80]. This motif has not previously been shown to be bound in ESCs in vivo, but is known to be important during neuronal differentiation[81]. Finally we rediscovered the *Oct4–Sox2* motif, in which the bases with high contribution scores correspond to the specific DNA contacts made by the heterodimer (based on the Oct1–Sox2 crystal structure)[53,82,83] (Fig. 3a). Thus, we discovered composite motifs that are consistent with known structural data.

We did not identify the composite *Sox2–Nanog* motif[71] and found no evidence that this motif was bound in our ChIP–nexus data (Supplementary Fig. 8a). Instead, we identified three *Nanog* motifs: *Nanog*, *Nanog-alt* and *Nanog-mix*, the last of which is partially similar to the first two. All have a main footprint around a

Fig. 2 | TF motifs and their genomic instances can be accurately derived from BPNet using interpretation tools. a, DeepLIFT recursively decomposes the predicted TF-specific binding output of the model and quantifies the contribution of each base of the input DNA sequence by backtracking its influence on the prediction through the network. **b**, Procedure for inferring and mapping predictive motif instances using the known distal *Oct4* enhancer (chr17:35504453–35504603) as an example. From the predicted ChIP–nexus profile for each TF (top), DeepLIFT derives TF-specific profile contribution scores (middle). Regions with high contribution scores (called seqlets) resemble TF-binding motifs. Seqlets are annotated by scanning the contribution scores with motifs discovered by TF–Modisco (bottom). **c**, To discover motifs, TF–Modisco scans for seqlets, extends the seqlets to 70 bp, performs pairwise alignments and clusters the seqlets. For each cluster, a motif is derived as CWM, obtained by averaging the contribution scores of each of the four bases at each position across all aligned seqlets. The corresponding PFM is the frequency of bases at each position. Motif instances are identified by scanning the CWM for each motif for high-scoring matches across profile contribution scores in the genomic regions. **d**, Example of a motif (N6) where the PFM differs from the CWMs. The PFM indicates that it is a repeat sequence (*RLTR9E*), while the CWM for each TF highlights the sequences that contribute to binding. **e**, Number of motif instances (in thousands) found in the ~150,000 genomic regions for the 11 representative motifs. **f**, Histogram of the number of mapped motif instances found per region. **g**, Evaluation of mapped motifs using previously identified regions that lose ATAC-seq signal in response to either Oct4 or Sox2 depletion (but not both)[77]. BPNet motif instances of *Oct4–Sox2* and *Sox2* (ranked by contribution scores) outperformed those obtained by HOMER and MEME (ranked by PWM match scores). **h**, A linear model based on the bottleneck layer of the trained BPNet model makes accurate quantitative predictions of the loss in ATAC-seq signal ($\log_{10}$ of the fold change) following depletion of Oct4 (ΔOct4) or Sox2 (ΔSox2). Results are shown with Pearson correlation coefficient (R_p) for test chromosomes 1, 8 and 9 that were held out during training. Supplementary Fig. 7b shows a similar model based on motif instance features.

TCA core sequence (Fig. 3b). Our primary *Nanog* motif resembles a previously identified *Nanog* motif from a thermodynamic model of ChIP–seq data[72]. Consistent with direct binding, a closely matching sequence (GCCATCA) is bound by Nanog in an EMSA gel shift assay[72]. *Nanog-alt* and *Nanog-mix* contain the sequence to which monomeric Nanog is bound in a crystal structure

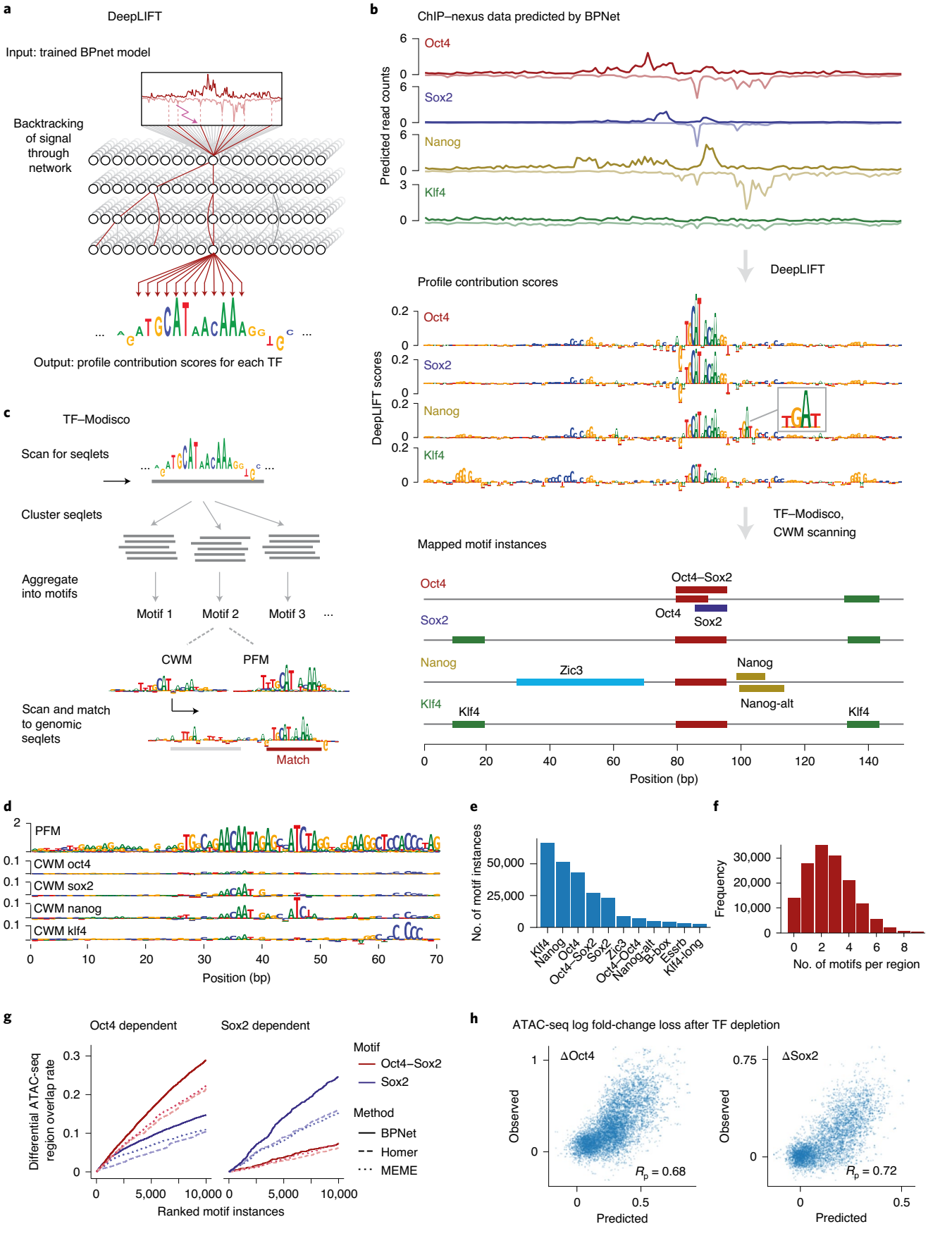

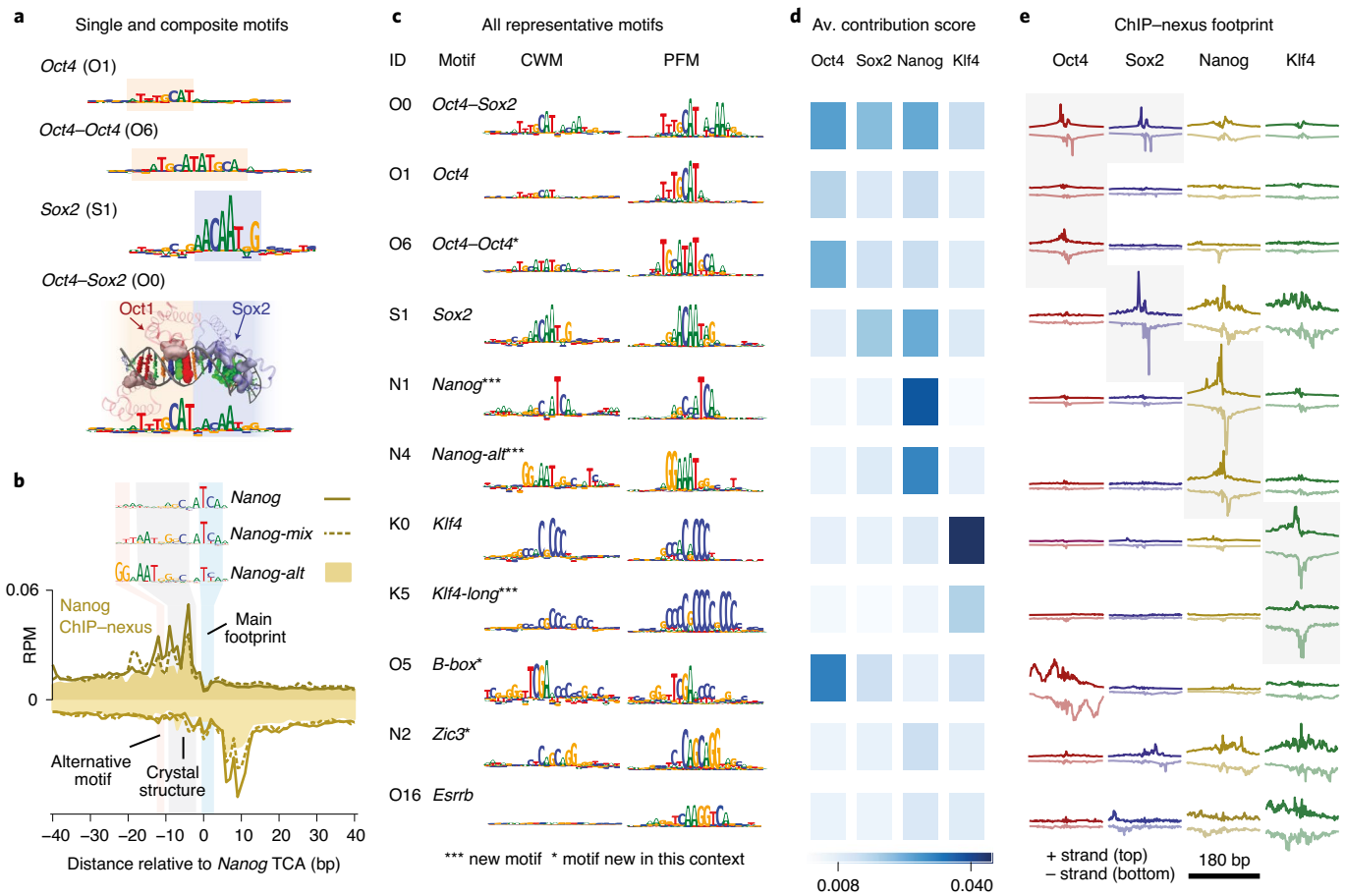

Fig. 3 | Discovery of composite motifs and indirect binding footprints. a, The CWMs of *Oct4*, *Oct4–Oct4*, *Sox2* and *Oct4–Sox2* were identified by TF-Modisco as separate motifs (motif IDs are the first letter of the TF+ number—for example, O1 discovered for Oct4), highlighting its ability to identify composite motifs. The CWM of the *Oct4–Sox2* composite motif correlates with the structure of Oct1 and Sox2 bound to the *Oct4–Sox2* motif. For visualization, the amino acids of Oct1 and Sox2 that contact DNA are shown as solid while the atoms in the DNA bases, shown as colored spheres, are sized according to the contribution scores shown in the CWM below. **b**, Nanog ChIP-nexus binding footprints were associated with three Nanog motif variants (shown as CWM). For all motifs, the main footprint was found at the TCA sequence. The CWMs of *Nanog-mix* (N5) and *Nanog-alt* (N4) contain a sequence that matches the sequence AATGGGC bound by Nanog in a crystal structure[84]. The CWM of *Nanog-alt* contains an alternative GG. **c**, The representative short motifs discovered contain known motifs, new motifs (***) and known motifs new in this context (*). All sequence logos share the same *y* axis. The *B-box* mediates RNA polymerase III transcription[117,118] and is associated with high levels of Oct4 binding upstream and downstream of tRNA (Extended Data Fig. 5e,f). **d**, The average (Av.) contribution score of the motif is shown for each TF. The highest score may indicate the TF that binds directly. **e**, The TF average ChIP-nexus footprint better indicates whether the motif is directly bound (sharp profile, marked with gray background), indirectly bound (fuzzy profile) or not bound at all. The footprints for each TF share the same *y* axis. RPM, reads per million.

(AATGGGC)[84]. Given these two separate direct DNA contacts, the observed Nanog binding footprint probably represents Nanog binding as a homodimer[85]. However, since *Nanog-alt* contains an additional GG to the left (Fig. 3b), we cannot rule out the existence of an unknown Nanog binding partner (but not Sox2 or Pbx; Supplementary Fig. 8b,c).

The majority of composite motifs, however, came from retrotransposons. This is consistent with previous observations that retrotransposons may contain multiple ancestral TF-binding sites[86–90] (Extended Data Fig. 5a). Among all motif pairs, the top 1% most frequent distances mapped in 83% of ERVs and were often >20 bp (Extended Data Fig. 5b and Supplementary Fig. 9), which exceeds the typical distance between motifs found in composite motifs that promote TF cooperativity[91,92]. This suggests that over-represented strict motif spacings alone are not a reliable indicator of functional motif syntax.

We next analyzed whether the 11 motifs showed evidence beyond strict motif spacings for mediation of cooperative TF interactions (Fig. 3c). By inspecting the contribution scores (Fig. 3d), we found that many motifs were predicted to contribute to the binding of other TFs. Moreover, we discovered motifs of pluripotency TFs that we had not profiled, including *Zic3* and *Esrrb*, which we validated with additional ChIP–nexus experiments (Extended Data Fig. 5c–f). Thus BPNet predicts that Oct4, Sox2, Nanog and Klf4 frequently bind, with the help of motifs from other TFs.

One explanation for this observation is that TFs may be indirectly recruited to motifs of other TFs[50,51]. We therefore inspected the average ChIP–nexus binding footprints of all TFs at all motifs (Fig. 3e). We found that TFs directly bound to their motifs showed sharp average ChIP–nexus footprints (marked in gray in Fig. 3e), but that TFs also showed broader, more fuzzy, footprints at other motifs, which we attribute to indirect binding. The level of indirect TF occupancy correlated with the contribution score for the TF (Fig. 3d,e), suggesting that indirect footprints are predicted by BPNet.

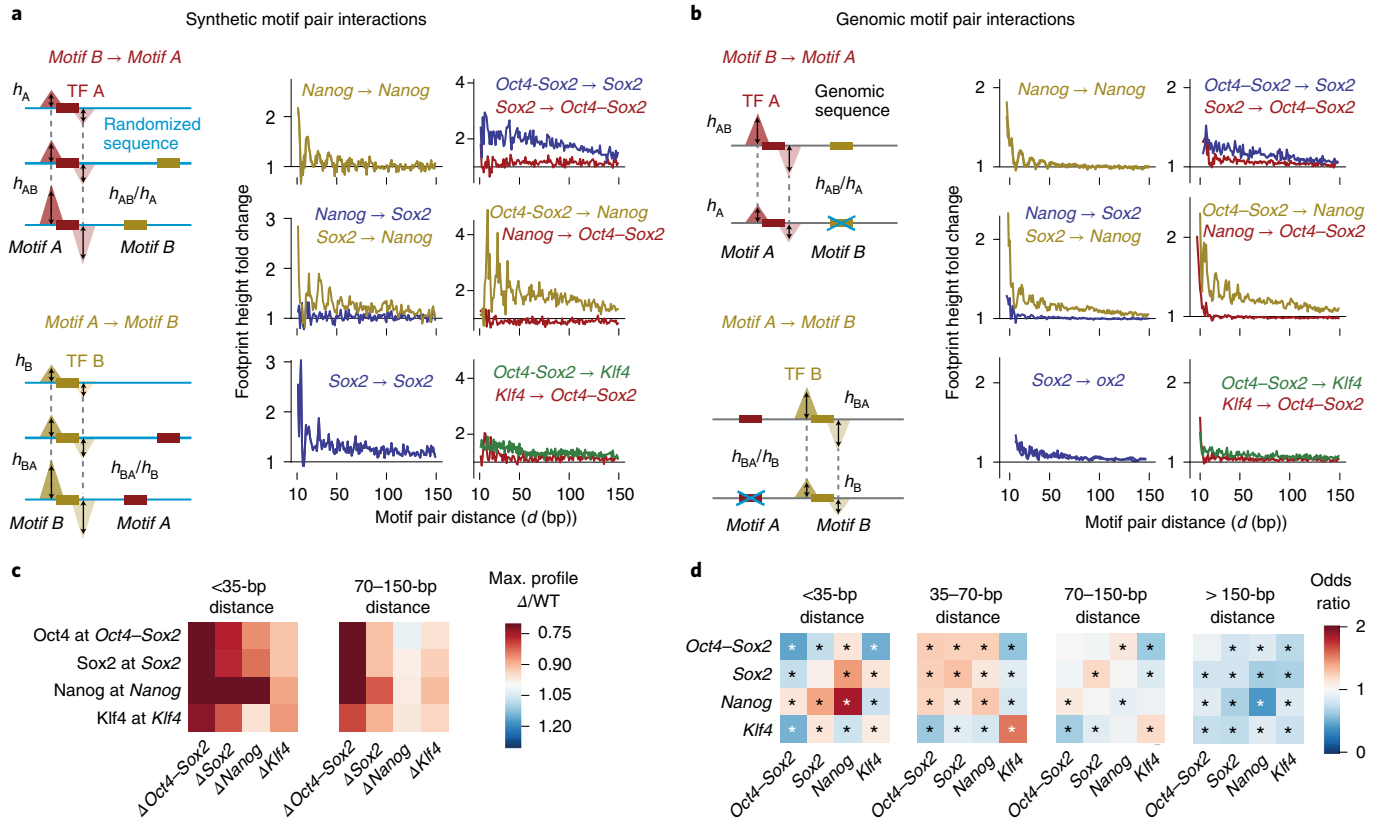

Fig. 4 | In silico motif interaction analysis reveals TF cooperativity and motif syntax. a, In the synthetic motif interaction analysis, *Motif A* is inserted into random sequences and the average profile for TF A is predicted by BPNet. The footprint summits are recorded (dotted lines) and the height (h_A) is measured at this position. *Motif B* is then inserted at a specific distance (*d*) from *Motif A* into a new set of random sequences and the average predicted footprint height is measured at the reference summit position (h_{AB} at dashed lines). The interaction of *Motif B* and *Motif A* as a function of *d* is quantified as the footprint height fold change (h_{AB}/h_A) after correction of h_{AB} for shoulder effects or indirect binding footprints from the nearby motif (Supplementary Fig. 10a). The interaction of *Motif A* and *Motif B* is obtained in an analogous way. The results show functions consistent with protein-range interactions between *Nanog* and *Sox2* or nucleosome-range interactions exerted by the *Oct4–Sox2* motif (bound by Oct4) on the binding of Sox2, Nanog or Klf4 on their respective motifs. Results are shown for the + + orientation of the two motifs (Supplementary Fig. 10c shows all motif pair orientations and Supplementary Fig. 10b shows the frequency of motif pairs). **b**, In genomic motif interaction analysis, naturally occurring instances of *Motif A* and *Motif B* as determined by CWM scanning were used. The average predicted footprint height and position of TF A were measured in the presence of *Motif B* (h_{AB}) and after replacement of *Motif B* with random bases (h_A at dashed lines). The same corrected footprint height fold change, h_{AB}/h_A or h_{BA}/h_B as a function of *d*, is used to quantify the interaction. The results from the average of all motif orientations are similar to those from synthetic motif interaction analysis. **c**, Quantification of the results shown in **b** as a heat map. Distances <35 bp are shown as representative for protein-range interactions, while 70–150 bp is representative for nucleosome-range interactions. **d**, Odds by which two motifs are found within a specified distance from each other, divided by the odds that both would be found in proximity by chance (observed by permutation of the region index). $^*P < 10^{-5}$ using Pearson's chi-squared test (Supplementary Methods). WT, wild type.

Notably, indirect footprints tended to occur in an asymmetric or directional manner (Fig. 3d,e). For example, Nanog was bound indirectly to the *Sox2* motif but Sox2 was not detected at the *Nanog* motif. Since Sox2 and Nanog have been shown to physically interact with each other[71,93], this suggests that these TFs indeed cooperate in some way but not through a composite motif. We therefore set out to systematically analyze how motif pairs influence cooperative binding, as a means to identify functional motif syntax.

Interpretation of BPNet reveals cooperative TF interactions. By training on base-resolution profiles, BPNet learned rules of TF cooperativity that we could extract by interrogating the trained model in silico like an oracle. We developed two complementary in silico motif interaction analysis approaches that measure how the binding of a TF to its motif is affected by a second motif as a function of their relative distance (Fig. 4, Extended Data Fig. 6 and Supplementary Fig. 10). We focused on the motifs most strongly bound by each of the four TFs: *Oct4–Sox2* (bound by Oct4), *Sox2*, *Nanog* and *Klf4*. The first approach uses synthetically designed sequences (Fig. 4a) while the second mutates naturally occurring nonoverlapping motifs in genomic sequences (Fig. 4b).

In the synthetic approach, *Motif A* is embedded in random DNA sequences and the BPNet model is used to predict the fold change in binding of TF A due to the addition of *Motif B* at a range of distances from *Motif A* (Fig. 4a and Supplementary Videos 1–6). The procedure is then repeated by anchoring *Motif B* and predicting the fold change in binding of TF B as a function of distance to *Motif A*. The robustness of the results was confirmed by the reproducibility of the patterns across five models trained independently on different subsets of regions (Supplementary Fig. 11).

Using the synthetic approach on all motif pair combinations, we observed distance-dependent cooperative TF interactions (Fig. 4a). These were distinct for each motif pair but independent of strand orientation (Supplementary Fig. 10b,c). For example, predicted Nanog binding at the *Nanog* motif was strongly enhanced when another *Nanog* motif was nearby but, interestingly, distance-dependent

enhancement exhibited a periodic pattern (Fig. 4a). A similar periodic binding dependency was observed for Nanog when a *Sox2* motif was nearby. The magnitude of this interaction was strongest at close distances (<35 bp), and thus could be mediated by either protein–protein interactions between Sox2 and Nanog[71,93] or DNA allostery[4,94]. For larger intermotif distances, the impact on Nanog binding rapidly diminished but was still elevated further away in the presence of a *Sox2* motif (but not a *Nanog* motif). This was not true the other way around, since Sox2 binding to its motif was not enhanced by a nearby *Nanog* motif (Fig. 4a). Thus, BPNet predicts that Sox2 and Nanog interact and that this cooperative interaction is directional, consistent with the indirect footprints we observed.

The motif interaction functions also suggested that the *Oct4–Sox2* motif mediates its effect through increased DNA accessibility in chromatin, consistent with Oct4 and Sox2 being pioneer TFs[73,77,95,96]. First, *Oct4–Sox2* strongly enhanced the predicted binding of Sox2, Nanog and, to a lesser extent, Klf4, at nucleosome-range distances of 150 bp (Fig. 4a). Second, these interactions were directional since the motifs of the other TFs did not substantially impact the predicted binding of Oct4 to the *Oct4–Sox2* motif, consistent with a hierarchical requirement for pioneer TFs to arrive first and make the region accessible for other TFs. Our results therefore suggest that motifs can be classified in a given context by their strength as pioneer motifs—that is, *Oct4–Sox2* is a stronger pioneer motif than *Sox2*.

We observed very similar distance-dependent cooperative interactions for all motif pairs using a complementary motif mutagenesis approach for genomic sequences (Fig. 4b and Extended Data Fig. 6). Here we used the original genomic sequences and predicted the binding profile of TF A to *Motif A* before and after replacement of *Motif B* with a random sequence (*Motif B* → *Motif A*) and vice versa. The effect sizes were less than in the synthetic approach, probably because the genomic motif instances were often of lower affinity than the ideal motifs used in the synthetic approach. It is also possible that motif mutations can be buffered by the additional motifs present in genomic sequences. However, the distance relationship and the directionality of the cooperative interactions were again very similar (Extended Data Fig. 6). These relationships can also be summarized as a heat map using distance intervals of <35 and 70–150 bp, which highlight the interactions in protein and nucleosome range, respectively (Fig. 4c).

These results suggest the existence of soft motif syntax: rather than requiring strict intermotif distances for cooperative binding, interactions between two motifs occur in a flexible but distance-dependent fashion that is specific for each motif pair. To obtain further evidence, we asked whether the preferred intermotif distances are observed in naturally occurring genomic regions. We removed retrotransposons containing strictly spaced motifs and analyzed whether motif pairs co-occur more frequently than expected by chance at certain distances (Fig. 4d and Supplementary Fig. 10b). The *Nanog* motifs were most strongly over-represented at short distances to *Sox2* and other *Nanog* motifs (<35 bp), consistent with their protein-range interactions. At nucleosome distance (70–150 bp) the *Oct4–Sox2* motif still co-occurred with *Nanog*, consistent with its pioneering role. Although BPNet is designed to capture potential motif interactions up to 1 kb apart, we did not identify significantly over-represented motif pairs beyond 150 bp (Fig. 4d). Altogether, we detected genome-wide soft preferences for motif spacings that correspond to some extent with detected cooperative binding interactions, and thus are probably functionally relevant soft motif syntax.

Nanog binding has a strong ~10.5-bp periodic pattern. The most remarkable soft motif syntax we observed was a ~10.5-bp periodicity associated with Nanog. We first observed periodicity in the full-length CWM of the *Nanog* motif, which showed flanking A/T bases in a periodic pattern (Fig. 5a). This pattern is not seen in the corresponding PFM representation, suggesting that A/T bases are not statistically over-represented but, when present, contribute strongly to Nanog binding predictions. The strong periodic pattern is confirmed in the individual contribution scores of *Nanog* motif instances, shown as a heat map and average contribution scores in Fig. 5b. A Fourier power spectrum analysis of contribution scores around the *Nanog* motif revealed strong periodicity averaging around 10.5 ± 0.3 bp (Fig. 5c), which falls within the observed 10–11-bp periodicity of the DNA helix observed both in vitro and in vivo[97–100]. This helical periodicity was also found for other motifs important for prediction of Nanog binding, including *Nanog-mix*, *Nanog-alt*, *Sox2*, *Oct4–Sox2 and Zic3*. However, the same motifs did not predict periodic binding for other TFs, suggesting that helical periodicity is specific for Nanog binding (Fig. 5d), consistent with its behavior in the in silico motif interaction analysis.

To obtain further evidence of this periodicity, we tested whether Nanog's soft syntax was naturally found in genomic DNA sequence. Indeed, the pairwise distance between our mapped *Nanog* motif instances showed a strong helical spacing preference for multiples of ~10.5 bp, independent of motif orientation (Fig. 5e). This periodicity was reproducibly inferred from five independent models on different subsets of the binding data (Supplementary Fig. 12a). Despite its presence in genomic DNA this pattern had not been discovered previously[47,67–72], presumably because it is difficult to detect with traditional methods and requires BPNet's large receptive field to learn motifs in a larger sequence context (Extended Data Fig. 7).

The in silico motif interaction analysis also predicted enhanced periodic binding cooperativity of Nanog in the presence of other motifs. In support of this, the mapped genomic distances between *Nanog* and either *Sox2* or *Oct4–Sox2* motif instances also showed strong preferred distances of helical periodicity regardless of motif orientation (Fig. 5f–g). This was also true for the distances between *Nanog* and *Zic3*, indicating that Zic3 is an additional interaction partner (Fig. 5h). Furthermore, the Nanog ChIP–nexus profiles themselves also showed this periodic pattern (Fig. 5i–k and Supplementary Figs. 12b and 13). The signal in the original data probably explains how BPNet was able to learn the preferred binding pattern of Nanog during training.

The helical periodicity suggests that Nanog binding is enhanced when the relevant partner motifs are found on the same side of the DNA. Since Nanog physically interacts with Sox2 (refs. [71,93]) and preferentially interacts at protein–protein distance in our in silico motif interaction analysis, it is possible that Nanog engages in cooperative protein–protein interactions similar to those observed for the lambda and lac repressors[101,102]. Alternatively, helical periodicity could be due to preferred binding of Nanog to nucleosomal DNA from the solvent surface, which has been observed for some homeodomain TFs[103,104].

Altogether, we identified helical periodicity as a strong cis-regulatory motif syntax for Nanog, a biophysical parameter on which BPNet was not explicitly trained. This result demonstrates the power of neural networks in discovering new patterns de novo without making explicit assumptions about the nature of the sequence features.

CRISPR validates the motif syntax between Nanog and Sox2. To experimentally validate the motif syntax identified by BPNet, we performed targeted point mutations in mapped motifs and compared the observed changes in ChIP–nexus profiles to those predicted by BPNet (Fig. 6). Since the most striking motif syntax was the helical periodicity of Nanog and the directional cooperativity with Sox2, and since the *Nanog* motif had previously been uncertain[47,67–72], we selected a genomic region that has a *Nanog* and a *Sox2* motif, as well as periodic Nanog binding. Using CRISPR/Cas9 and homologous recombination, we performed two-base substitutions

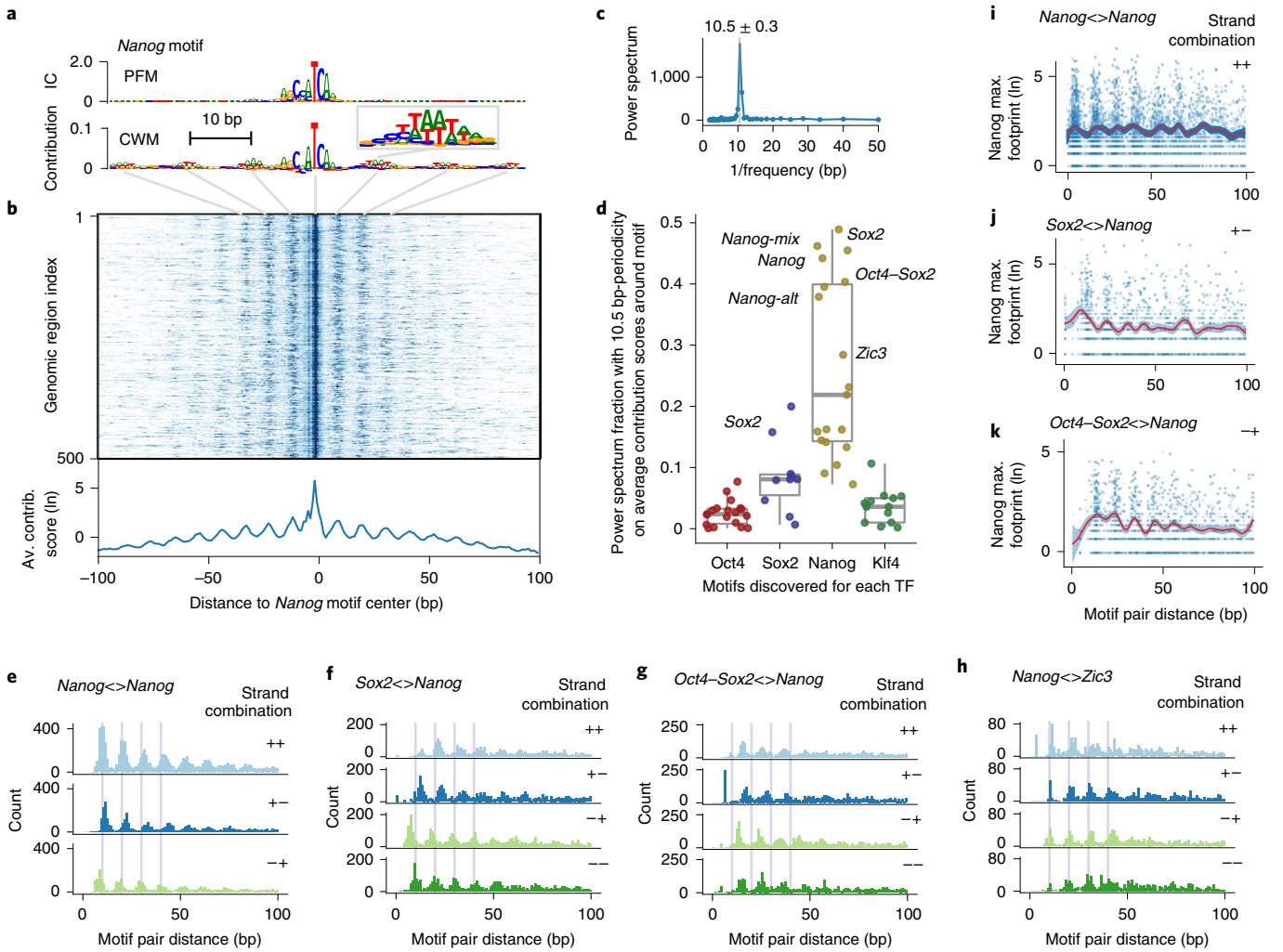

Fig. 5 | Pervasive helical periodicity between Nanog and partner motifs. a, The CWM, but not the PFM, of the main *Nanog* motif has periodically occurring contributing bases in the flanks (example in enlarged window). **b**, Heat map of contribution (Contrib.) scores of individual Nanog instances also shows this periodic pattern, the average (Av.) of which is shown below. **c**, Fourier power spectrum of average contribution score around *Nanog* motif instances (after subtraction of the smoothed signal) reveals an average periodicity of 10.5 ± 0.3 bp. **d**, Fraction of the power spectrum with 10.5-bp periodicity of average contribution scores around the motifs discovered for each TF (19 for Oct4, 10 for Sox2, 19 for Nanog and 13 for Klf4) shows that helical periodicity is specific for Nanog binding. Important motifs are labeled; unlabeled high-scoring motifs are derived from retrotransposons. The box plots mark the median, upper and lower quartiles and 1.5× interquartile range (whiskers). **e**, Pairwise spacing of *Nanog* motif instances in all possible orientations also show a periodic pattern (+ + includes the – – orientation). **f**–**h**, Heterologous motif combinations of *Nanog* with *Sox2* (**f**), *Oct4–Sox2* (**g**) and *Zic3* (**h**) also show a preferred spacing with the same periodicity. The distance between two motifs is always kept positive by placing the second in the pair downstream of the first. All four motif orientations are considered: +, the motif lies on the forward strand; –, the motif lies on the reverse strand. **i**–**k**, Nanog ChIP–nexus signal at the reference summit position for each motif instance across every motif pair (blue dots), with the smooth curve fit (B-splines) depicted as a red line and 95% confidence intervals depicted as blue ribbons. Numbers of data points used to estimate 50 smoothing parameters for each plot: 8,930 for *Nanog*<>*Nanog* (**i**), 4,011 for *Sox2*<>*Nanog* (**j**) and 4,947 for *Oct4–Sox2*<>*Nanog* (**k**). Nanog on average binds higher when *Nanog* motifs have the preferred intermotif distance.

in either the *Sox2* motif (TTG to AGG) or the *Nanog* motif (TGA to GGC). We then performed Sox2 and Nanog ChIP–nexus experiments on wild-type and mutant ESCs using three independently derived clones per motif mutation. All replicate experiments were highly correlated and possessed indistinguishable normalized binding profiles and counts across known enhancers (Extended Data Fig. 8 and Supplementary Fig. 14).

We then examined how binding profiles were affected by mutations. As expected, mutation of the *Sox2* motif specifically abolished the corresponding Sox2 binding footprint (Fig. 6a). However, mutation of the *Nanog* motif did not affect Sox2 binding (Fig. 6b) while mutation of the *Sox2* motif strongly affected Nanog binding (Extended Data Fig. 8b). Nanog binding was almost completely lost near the *Sox2* mutation, and was still reduced at the nearby *Nanog* motif (Fig. 6c).

This directional cooperativity is strikingly consistent with the results from the in silico motif interaction analysis performed across all genomic sequences (Fig. 4b), and with the asymmetry observed in the indirect binding footprints of Nanog and Sox2 (Fig. 3c). In addition, the short-range cooperativity of Nanog was confirmed. Namely, when the *Nanog* motif was mutated, not only was the corresponding footprint of Nanog abrogated as expected but the surrounding periodic Nanog binding was also reduced as predicted (Fig. 6d).

Altogether, these results confirm that the derived syntax rules are predictive and applicable to individual examples, demonstrating that BPNet can be used to derive new, testable biological

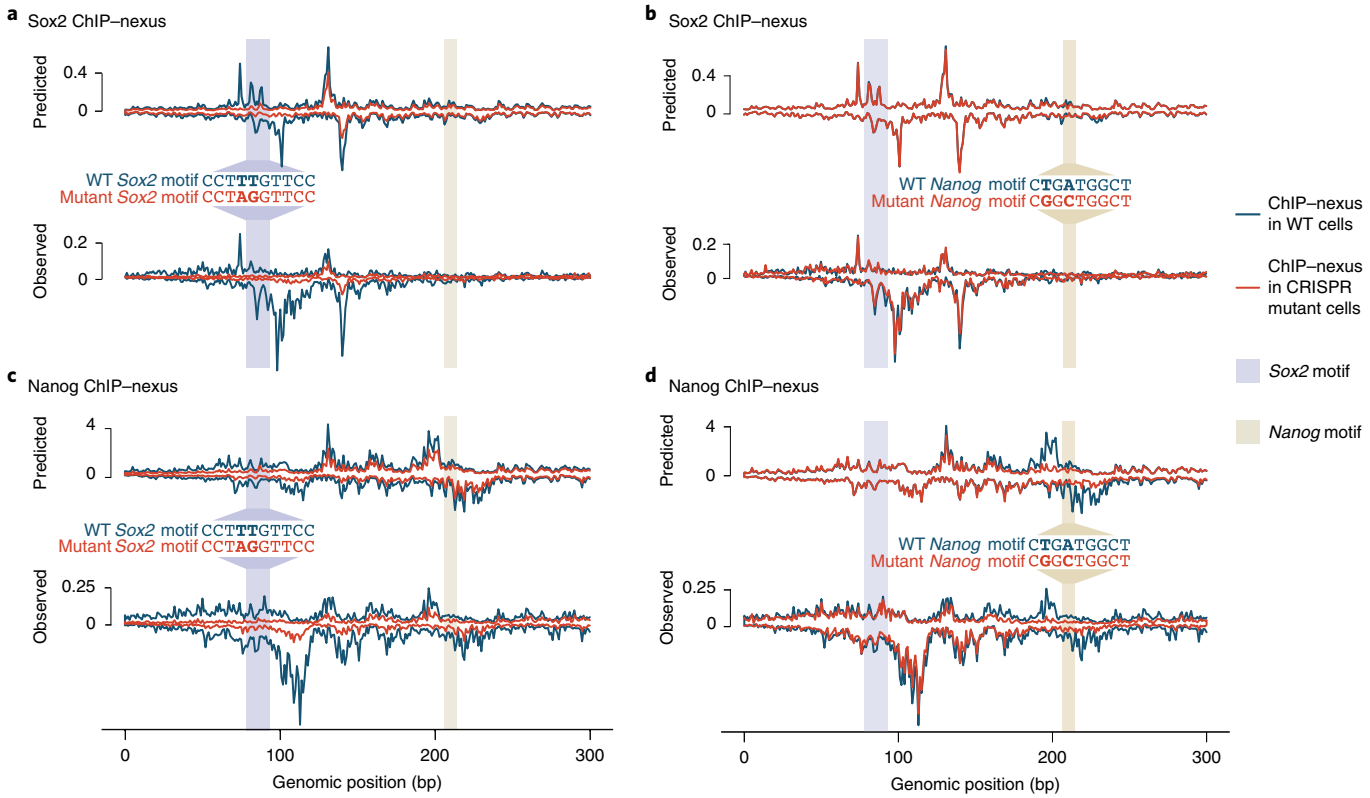

Fig. 6 | CRISPR mutations in a Sox2 and a Nanog motif validate BPNet predictions. a–d, A *Sox2* and a *Nanog* motif in a selected genomic region were mutated through CRISPR/Cas9 and homologous recombination in mouse ESCs. Predicted and observed ChIP–nexus profiles (+, strand above zero; –, strand below zero) in reads per million are shown for wild-type (WT) and mutant cells across 300 bp (chr10:85,539,550–85,539,850). **a**, Following mutation of the *Sox2* motif, the Sox2 footprint was lost as predicted. **b**, In contrast, mutation of the *Nanog* motif did not noticeably affect Sox2 binding. **c**, Consistent with directional cooperativity, the *Sox2* motif mutation did, however, affect Nanog binding, which was reduced throughout the region as predicted. **d**, Similarly, mutation of the *Nanog* motif not only abrogated the Nanog footprint but also resulted in reduced binding nearby as predicted. Extended Data Fig. 8 and Supplementary Fig. 14 illustrate reproducibility validations.

hypotheses on how the cis-regulatory motif syntax influences TF binding.

Discussion

Here we introduce BPNet, a versatile and interpretable deep learning tool to learn TF motifs and the rules of syntax that best predict experimental data at base resolution. To leverage the unprecedented resolution of BPNet and showcase its ability to reveal new biological insights, we applied it to ChIP–nexus data in ESCs. The results were not only consistent with previous findings, but revealed new details and principles of cis-regulatory motif syntax. We found that TF binding is guided by soft syntax rules, which follow clear intermotif, distance-dependent relationships consistent with protein–protein interactions[16,105] or nucleosome-mediated cooperativity[106]. Such soft syntax rules represent an intermediate between the strict motif syntax associated with the original enhanceosome model[107,108] and the very flexible syntax suggested by the billboard model[14]. The TF cooperativity associated with specific motif pairs was often directional and consistent with motifs mediating the role of pioneer TFs with different strengths. Finally, we observed a strong preference for Nanog to bind with ~10.5-bp helical periodicity. Helical periodicity has long been thought to be a potential element of the cis-regulatory code[25,27,101,102,107,109–112]. Our finding that the helical periodicity is motif encoded and TF specific provides a guidance for identifying this feature for other TFs in the future.

As we outline below, BPNet represents a paradigm for discovering relevant motifs and syntax rules underlying the cis-regulatory code. Through several important design innovations (Supplementary Note), as well as extensive quality control and rigorous evaluations to ensure that the method works as intended, BPNet outperforms both traditional methods and previous deep learning models (Supplementary Note). BPNet outperforms traditional methods because it infers predictive patterns in a larger sequence context and is not reliant on over-represented sequence patterns. BPNet outperforms previous neural networks by modeling TF binding profiles at base resolution, which enables it to learn subtle cooperative interactions between motifs (Extended Data Fig. 4). The result is a powerful and general computational framework for deciphering the cis-regulatory code from a variety of genomics assays.

An important innovation was the development of tools that make the trained BPNet model interpretable. Computational models in regulatory genomics have long grappled with an inherent trade-off between prediction accuracy and interpretability, but the BPNet framework enables both. The key to enhancing interpretability was the distillation of predictive motif representations and context-aware motif instances from the entire neural network, rather than direct interpretation of millions of cryptic, partially redundant, parameters of the trained model. Importantly, by using BPNet as an in silico oracle, we systematically predicted the effect of mutated sequences or synthetic sequence designs, which enables us to extract the influence of pairwise motif spacing on TF cooperativity. The precise oracle predictions, which are not possible with classical models, allow less scalable in vivo experiments such as the CRISPR editing experiments to be performed on the most interesting and promising observations.

The advantage of BPNet over classical methods is that it detects motifs and their syntax in a fundamentally different way. Classical methods for motif discovery rely on motifs being over-represented compared to background sequences[18–21]. Similarly, existing approaches to infer syntax rules use summary statistics of over-represented co-occurrence patterns[1,23,113]. These methods have limited statistical power to test individual features present in complex cis-regulatory sequences (Supplementary Note). By contrast, BPNet's vast network capacity allows it to learn complex predictive rules agnostically based on their ability to accurately predict relevant experimental profiles, without explicitly defining features a priori. This allows the discovery of relatively rare but nonetheless predictive motifs (for example, *Oct4–Oct4*), as well as predictive syntax features, such as helical periodicity or the direction of TF cooperativity, that were not known to be relevant for these TFs.

The BPNet approach of modeling the entire cis-regulatory sequence is better suited for deciphering the combinatorial requirements for TF binding in vivo. Traditionally, a TF-binding site is defined by its strong affinity in in vitro experiments or by statistically significant sequence matches to PWM models. In both cases, a selection is typically made by arbitrary thresholds before the role of motif combinations, syntax and sequence context is considered[113,114]. However, our results suggest that, in vivo, TF binding to a motif instance is by itself a highly cooperative process that depends on neighboring motifs and syntax. Indeed, this explains how enhancer function can be critically dependent on low-affinity binding sites[10,52,115]. The fact that BPNet discovered subtle predictive patterns that are not strong matches to PWM motif models (for example, the predictive bases in the flanks of *Nanog* motifs), and outperformed classical methods for identification of motif instances relevant in vivo (Fig. 2g–h and Supplementary Note), suggests that modeling putative motif instances within their cis-regulatory context is an important advantage.

Finally, BPNet is designed to be a general and versatile end-to-end approach adaptable to a number of genomic assays. It is ideally suited to learn from high-resolution genomic data, but its base-resolution output is still beneficial for lower-resolution data since it does not discard any information present in the training data profiles. For example, we successfully trained BPNet models on ChIP–seq profiles for the same TFs and obtained motifs that were highly similar, including a periodic *Nanog* motif (Extended Data Figs. 9 and 10 and Supplementary Note). The number and accuracy of motif instances were lower than those from ChIP–nexus profile models, but better than those from models trained on coarse-resolution binary binding labels (Extended Data Fig. 10c,d). Similarly, we found that BPNet can accurately model base-resolution DNase-seq profiles[116]. This suggests that the application of BPNet to existing compendia of ChIP–seq, DNase-seq and ATAC-seq data, such as those generated by ENCODE, will improve the systematic mapping of cis-regulatory motifs and their rules of syntax in a variety of cellular contexts. To foster the broad application of BPNet, we have made the entire software framework available with documentation and tutorials.

Learning motifs and syntax-dependent regulatory influence for a variety of genomic assays in many cell types will build a more complete understanding of the cis-regulatory code and reveal how specific bases influence the various molecular steps associated with enhancer function. At the same time, these models will provide opportunities to pinpoint causal quantitative trait- and disease-associated genetic variants and understand the molecular mechanisms by which they alter gene regulation. Ultimately, the ability to decipher the cis-regulatory code will unlock an enormous amount of information underlying organismal development and its maintenance, and pinpoint therapeutic intervention opportunities for diseases.

Online content

Any methods, additional references, Nature Research reporting summaries, source data, extended data, supplementary information, acknowledgements, peer review information; details of author contributions and competing interests; and statements of data and code availability are available at https://doi.org/10.1038/s41588-021-00782-6.

Received: 19 July 2020; Accepted: 7 January 2021;
Published online: 18 February 2021

References

1. Gerstein, M. B. et al. Architecture of the human regulatory network derived from ENCODE data. *Nature* **489**, 91–100 (2012).
2. ENCODE Project Consortium. An integrated encyclopedia of DNA elements in the human genome. *Nature* **489**, 57–74 (2012).
3. Roadmap Epigenomics Consortiumet al. Integrative analysis of 111 reference human epigenomes. *Nature* **518**, 317–330 (2015).
4. Morgunova, E. & Taipale, J. Structural perspective of cooperative transcription factor binding. *Curr. Opin. Struct. Biol.* **47**, 1–8 (2017).
5. Zinzen, R. P., Senger, K., Levine, M. & Papatsenko, D. Computational models for neurogenic gene expression in the *Drosophila* embryo. *Curr. Biol.* **16**, 1358–1365 (2006).
6. Fiore, C. & Cohen, B. A. Interactions between pluripotency factors specify cis-regulation in embryonic stem cells. *Genome Res.* **26**, 778–786 (2016).
7. Sayal, R., Dresch, J. M., Pushel, I., Taylor, B. R. & Arnosti, D. N. Quantitative perturbation-based analysis of gene expression predicts enhancer activity in early *Drosophila* embryo. *eLife* **5**, e08445 (2016).
8. Erceg, J. et al. Subtle changes in motif positioning cause tissue-specific effects on robustness of an enhancer's activity. *PLoS Genet.* **10**, e1004060 (2014).
9. Crocker, J. & Ilsley, G. R. Using synthetic biology to study gene regulatory evolution. *Curr. Opin. Genet. Dev.* **47**, 91–101 (2017).
10. Farley, E. K. et al. Suboptimization of developmental enhancers. *Science* **350**, 325–328 (2015).
11. Swanson, C. I., Evans, N. C. & Barolo, S. Structural rules and complex regulatory circuitry constrain expression of a Notch- and EGFR-regulated eye enhancer. *Dev. Cell* **18**, 359–370 (2010).
12. Liu, F. & Posakony, J. W. Role of architecture in the function and specificity of two Notch-regulated transcriptional enhancer modules. *PLoS Genet.* **8**, e1002796 (2012).
13. Lusk, R. W. & Eisen, M. B. Evolutionary mirages: selection on binding site composition creates the illusion of conserved grammars in *Drosophila* enhancers. *PLoS Genet.* **6**, e1000829 (2010).
14. Kulkarni, M. M. & Arnosti, D. N. Information display by transcriptional enhancers. *Development* **130**, 6569–6575 (2003).
15. Liberman, L. M. & Stathopoulos, A. Design flexibility in cis-regulatory control of gene expression: synthetic and comparative evidence. *Dev. Biol.* **327**, 578–589 (2009).
16. Junion, G. et al. A transcription factor collective defines cardiac cell fate and reflects lineage history. *Cell* **148**, 473–486 (2012).
17. King, D. M. et al. Synthetic and genomic regulatory elements reveal aspects of cis-regulatory grammar in mouse embryonic stem cells. *eLife* **9**, e41279 (2020).
18. Bailey, T. L. et al. MEME SUITE: tools for motif discovery and searching. *Nucleic Acids Res.* **37**, W202–W208 (2009).
19. Hughes, J. D., Estep, P. W., Tavazoie, S. & Church, G. M. Computational identification of cis-regulatory elements associated with groups of functionally related genes in *Saccharomyces cerevisiae*. *J. Mol. Biol.* **296**, 1205–1214 (2000).
20. Pavesi, G., Mereghetti, P., Mauri, G. & Pesole, G. Weeder Web: discovery of transcription factor binding sites in a set of sequences from co-regulated genes. *Nucleic Acids Res.* **32**, W199–W203 (2004).
21. Thijs, G. et al. A higher-order background model improves the detection of promoter regulatory elements by Gibbs sampling. *Bioinformatics* **17**, 1113–1122 (2001).
22. Cheng, Q. et al. Computational identification of diverse mechanisms underlying transcription factor-DNA occupancy. *PLoS Genet.* **9**, e1003571 (2013).
23. Guo, Y., Mahony, S. & Gifford, D. K. High resolution genome wide binding event finding and motif discovery reveals transcription factor spatial binding constraints. *PLoS Comput. Biol.* **8**, e1002638 (2012).
24. Wang, J. et al. Sequence features and chromatin structure around the genomic regions bound by 119 human transcription factors. *Genome Res.* **22**, 1798–1812 (2012).
25. Lee, D., Karchin, R. & Beer, M. A. Discriminative prediction of mammalian enhancers from DNA sequence. *Genome Res.* **21**, 2167–2180 (2011).

26. Erives, A. & Levine, M. Coordinate enhancers share common organizational features in the *Drosophila* genome. *Proc. Natl Acad. Sci. USA* **101**, 3851–3856 (2004).
27. Papatsenko, D., Goltsev, Y. & Levine, M. Organization of developmental enhancers in the *Drosophila* embryo. *Nucleic Acids Res.* **37**, 5665–5677 (2009).
28. Ng, F. S. L. et al. Constrained transcription factor spacing is prevalent and important for transcriptional control of mouse blood cells. *Nucleic Acids Res.* **42**, 13513–13524 (2014).
29. Kharchenko, P. V., Tolstorukov, M. Y. & Park, P. J. Design and analysis of ChIP–seq experiments for DNA-binding proteins. *Nat. Biotechnol.* **26**, 1351–1359 (2008).
30. Zhang, Y. et al. Model-based analysis of ChIP–seq (MACS). *Genome Biol.* **9**, R137 (2008).
31. Rozowsky, J. et al. PeakSeq enables systematic scoring of ChIP–seq experiments relative to controls. *Nat. Biotechnol.* **27**, 66–75 (2009).
32. Guo, Y. et al. Discovering homotypic binding events at high spatial resolution. *Bioinformatics* **26**, 3028–3034 (2010).
33. Kuan, P. F. et al. A statistical framework for the analysis of ChIP–seq data. *J. Am. Stat. Assoc.* **106**, 891–903 (2011).
34. Hartonen, T., Sahu, B., Dave, K., Kivioja, T. & Taipale, J. PeakXus: comprehensive transcription factor binding site discovery from ChIP–Nexus and ChIP–Exo experiments. *Bioinformatics* **32**, i629–i638 (2016).
35. Alipanahi, B., Delong, A., Weirauch, M. T. & Frey, B. J. Predicting the sequence specificities of DNA- and RNA-binding proteins by deep learning. *Nat. Biotechnol.* **33**, 831–838 (2015).
36. Zhou, J. & Troyanskaya, O. G. Predicting effects of noncoding variants with deep learning-based sequence model. *Nat. Methods* **12**, 931–934 (2015).
37. Quang, D. & Xie, X. FactorNet: a deep learning framework for predicting cell type specific transcription factor binding from nucleotide-resolution sequential data. *Methods* **166**, 40–47 (2019).
38. Bogard, N., Linder, J., Rosenberg, A. B. & Seelig, G. A deep neural network for predicting and engineering alternative polyadenylation. *Cell* **178**, 91–106 (2019).
39. Kelley, D. R., Snoek, J. & Rinn, J. L. Basset: learning the regulatory code of the accessible genome with deep convolutional neural networks. *Genome Res.* **26**, 990–999 (2016).
40. Lanchantin, J., Singh, R., Wang, B. & Qi, Y. Deep motif dashboard: visualizing and understanding genomic sequences using deep neural networks. *Pac. Symp. Biocomput.* **22**, 254–265 (2017).
41. Shrikumar, A. et al. TF-MoDISco v0.4.2.2-alpha: technical note. Preprint at *arXiv* https://arxiv.org/abs/1811.00416 (2018).
42. Jha, A., Aicher, J. K., Singh, D. & Barash, Y. Improving interpretability of deep learning models: splicing codes as a case study. Preprint at *bioRxiv* https://doi.org/10.1101/700096 (2019).
43. Greenside, P., Shimko, T., Fordyce, P. & Kundaje, A. Discovering epistatic feature interactions from neural network models of regulatory DNA sequences. *Bioinformatics* **34**, i629–i637 (2018).
44. Kelley, D. R. et al. Sequential regulatory activity prediction across chromosomes with convolutional neural networks. *Genome Res.* **28**, 739–750 (2018).
45. Gordân, R., Hartemink, A. J. & Bulyk, M. L. Distinguishing direct versus indirect transcription factor-DNA interactions. *Genome Res.* **19**, 2090–2100 (2009).
46. Mariani, L., Weinand, K., Vedenko, A., Barrera, L. A. & Bulyk, M. L. Identification of human lineage-specific transcriptional coregulators enabled by a glossary of binding modules and tunable genomic backgrounds. *Cell Syst.* **5**, 187–201 (2017).
47. Bailey, T. L. & Machanick, P. Inferring direct DNA binding from ChIP–seq. *Nucleic Acids Res.* **40**, e128 (2012).
48. Rhee, H. S. & Pugh, B. F. Comprehensive genome-wide protein–DNA interactions detected at single-nucleotide resolution. *Cell* **147**, 1408–1419 (2011).
49. He, Q., Johnston, J. & Zeitlinger, J. ChIP–nexus enables improved detection of in vivo transcription factor binding footprints. *Nat. Biotechnol.* **33**, 395–401 (2015).
50. Yamada, N., Lai, W. K. M., Farrell, N., Pugh, B. F. & Mahony, S. Characterizing protein–DNA binding event subtypes in ChIP–exo data. *Bioinformatics* **35**, 903–913 (2019).
51. Starick, S. R. et al. ChIP–exo signal associated with DNA-binding motifs provides insight into the genomic binding of the glucocorticoid receptor and cooperating transcription factors. *Genome Res.* **25**, 825–835 (2015).
52. Papagianni, A. et al. Capicua controls Toll/IL-1 signaling targets independently of RTK regulation. *Proc. Natl Acad. Sci. USA* **115**, 1807–1812 (2018).
53. Reményi, A. et al. Crystal structure of a POU/HMG/DNA ternary complex suggests differential assembly of Oct4 and Sox2 on two enhancers. *Genes Dev.* **17**, 2048–2059 (2003).
54. Banerji, J., Rusconi, S. & Schaffner, W. Expression of a beta-globin gene is enhanced by remote SV40 DNA sequences. *Cell* **27**, 299–308 (1981).
55. Spitz, F. & Furlong, E. E. M. Transcription factors: from enhancer binding to developmental control. *Nat. Rev. Genet.* **13**, 613–626 (2012).
56. Jaganathan, K. et al. Predicting splicing from primary sequence with deep learning. *Cell* **176**, 535–548 (2019).
57. He, K., Zhang, X., Ren, S. & Sun, J. Deep residual learning for image recognition. In *IEEE Conference on Computer Vision and Pattern Recognition (CVPR)* (eds. He, K. et al.) 770–778 (IEEE, 2016); https://doi.org/10.1109/CVPR.2016.90
58. Van Den Oord, A. & Dieleman, S. WaveNet: a generative model for raw audio. *DeepMind* https://deepmind.com/blog/article/wavenet-generative-model-raw-audio (2016).
59. Terooatea, T. W., Pozner, A. & Buck-Koehntop, B. A. PAtCh-Cap: input strategy for improving analysis of ChIP–exo data sets and beyond. *Nucleic Acids Res.* **44**, e159 (2016).
60. Whyte, W. A. et al. Enhancer decommissioning by LSD1 during embryonic stem cell differentiation. *Nature* **482**, 221–225 (2012).
61. Novo, C. L. et al. Long-range enhancer interactions are prevalent in mouse embryonic stem cells and are reorganized upon pluripotent state transition. *Cell Rep.* **22**, 2615–2627 (2018).
62. Festuccia, N. et al. Esrrb extinction triggers dismantling of naïve pluripotency and marks commitment to differentiation. *EMBO J.* **37**, e95476 (2018).
63. Moorthy, S. D. et al. Enhancers and super-enhancers have an equivalent regulatory role in embryonic stem cells through regulation of single or multiple genes. *Genome Res.* **27**, 246–258 (2017).
64. Avsec, Ž. et al. The Kipoi repository accelerates community exchange and reuse of predictive models for genomics. *Nat. Biotechnol.* **37**, 592–600 (2019).
65. Shrikumar, A., Greenside, P. & Kundaje, A. Learning important features through propagating activation differences. In *Proc. 34th International Conference on Machine Learning* 3145–3153 (2017).
66. Chew, J.-L. et al. Reciprocal transcriptional regulation of Pou5f1 and Sox2 via the Oct4/Sox2 complex in embryonic stem cells. *Mol. Cell. Biol.* **25**, 6031–6046 (2005).
67. Chen, X. et al. Integration of external signaling pathways with the core transcriptional network in embryonic stem cells. *Cell* **133**, 1106–1117 (2008).
68. Mitsui, K. et al. The homeoprotein Nanog is required for maintenance of pluripotency in mouse epiblast and ES cells. *Cell* **113**, 631–642 (2003).
69. Loh, Y.-H. et al. The Oct4 and Nanog transcription network regulates pluripotency in mouse embryonic stem cells. *Nat. Genet.* **38**, 431–440 (2006).
70. Salmon-Divon, M., Dvinge, H., Tammoja, K. & Bertone, P. PeakAnalyzer: genome-wide annotation of chromatin binding and modification loci. *BMC Bioinformatics* **11**, 415 (2010).
71. Gagliardi, A. et al. A direct physical interaction between Nanog and Sox2 regulates embryonic stem cell self-renewal. *EMBO J.* **32**, 2231–2247 (2013).
72. He, X. et al. A biophysical model for analysis of transcription factor interaction and binding site arrangement from genome-wide binding data. *PLoS ONE* **4**, e8155 (2009).
73. Xie, L. et al. A dynamic interplay of enhancer elements regulates Klf4 expression in naïve pluripotency. *Genes Dev.* **31**, 1795–1808 (2017).
74. Mistri, T. K. et al. Dynamic changes in Sox2 spatio-temporal expression promote the second cell fate decision through Fgf4/Fgfr2 signaling in preimplantation mouse embryos. *Biochem. J.* **475**, 1075–1089 (2018).
75. Tokuzawa, Y. et al. Fbx15 is a novel target of Oct3/4 but is dispensable for embryonic stem cell self-renewal and mouse development. *Mol. Cell. Biol.* **23**, 2699–2708 (2003).
76. Heinz, S. et al. Simple combinations of lineage-determining transcription factors prime cis-regulatory elements required for macrophage and B cell identities. *Mol. Cell* **38**, 576–589 (2010).
77. Friman, E. T. et al. Dynamic regulation of chromatin accessibility by pluripotency transcription factors across the cell cycle. *eLife* **8**, e5008 (2019).
78. Jolma, A. et al. DNA-binding specificities of human transcription factors. *Cell* **152**, 327–339 (2013).
79. Tomilin, A. et al. Synergism with the coactivator OBF-1 (OCA-B, BOB-1) is mediated by a specific POU dimer configuration. *Cell* **103**, 853–864 (2000).
80. Botquin, V. et al. New POU dimer configuration mediates antagonistic control of an osteopontin preimplantation enhancer by Oct-4 and Sox-2. *Genes Dev.* **12**, 2073–2090 (1998).
81. Mistri, T. K. et al. Selective influence of Sox2 on POU transcription factor binding in embryonic and neural stem cells. *EMBO Rep.* **16**, 1177–1191 (2015).
82. Ambrosetti, D. C., Basilico, C. & Dailey, L. Synergistic activation of the fibroblast growth factor 4 enhancer by Sox2 and Oct-3 depends on protein–protein interactions facilitated by a specific spatial arrangement of factor binding sites. *Mol. Cell. Biol.* **17**, 6321–6329 (1997).

83. Merino, F., Bouvier, B. & Cojocaru, V. Cooperative DNA recognition modulated by an interplay between protein–protein interactions and DNA-mediated allostery. *PLoS Comput. Biol.* **11**, e1004287 (2015).
84. Hayashi, Y. et al. Structure-based discovery of NANOG variant with enhanced properties to promote self-renewal and reprogramming of pluripotent stem cells. *Proc. Natl Acad. Sci. USA* **112**, 4666–4671 (2015).
85. Wang, J., Levasseur, D. N. & Orkin, S. H. Requirement of Nanog dimerization for stem cell self-renewal and pluripotency. *Proc. Natl Acad. Sci. USA* **105**, 6326–6331 (2008).
86. Todd, C. D., Deniz, Ö., Taylor, D. & Branco, M. R. Functional evaluation of transposable elements as enhancers in mouse embryonic and trophoblast stem cells. *eLife* **8**, e44344 (2019).
87. Bourque, G. et al. Evolution of the mammalian transcription factor binding repertoire via transposable elements. *Genome Res.* **18**, 1752–1762 (2008).
88. Kunarso, G. et al. Transposable elements have rewired the core regulatory network of human embryonic stem cells. *Nat. Genet.* **42**, 631–634 (2010).
89. Sundaram, V. et al. Functional cis-regulatory modules encoded by mouse-specific endogenous retrovirus. *Nat. Commun.* **8**, 14550 (2017).
90. Xie, D. et al. Rewirable gene regulatory networks in the preimplantation embryonic development of three mammalian species. *Genome Res.* **20**, 804–815 (2010).
91. Jankowski, A., Szczurek, E., Jauch, R., Tiuryn, J. & Prabhakar, S. Comprehensive prediction in 78 human cell lines reveals rigidity and compactness of transcription factor dimers. *Genome Res.* **23**, 1307–1318 (2013).
92. Jolma, A. et al. DNA-dependent formation of transcription factor pairs alters their binding specificity. *Nature* **527**, 384–388 (2015).
93. Mullin, N. P. et al. Distinct contributions of tryptophan residues within the dimerization domain to Nanog function. *J. Mol. Biol.* **429**, 1544–1553 (2017).
94. Kim, S. et al. Probing allostery through DNA. *Science* **339**, 816–819 (2013).
95. Soufi, A. et al. Pioneer transcription factors target partial DNA motifs on nucleosomes to initiate reprogramming. *Cell* **161**, 555–568 (2015).
96. Soufi, A., Donahue, G. & Zaret, K. S. Facilitators and impediments of the pluripotency reprogramming factors' initial engagement with the genome. *Cell* **151**, 994–1004 (2012).
97. Winter, D. R., Song, L., Mukherjee, S., Furey, T. S. & Crawford, G. E. DNase-seq predicts regions of rotational nucleosome stability across diverse human cell types. *Genome Res.* **23**, 1118–1129 (2013).
98. Zhong, J. et al. Mapping nucleosome positions using DNase-seq. *Genome Res.* **26**, 351–364 (2016).
99. Jin, H., Rube, H. T. & Song, J. S. Categorical spectral analysis of periodicity in nucleosomal DNA. *Nucleic Acids Res.* **44**, 2047–2057 (2016).
100. Drew, H. R. et al. Structure of a B-DNA dodecamer: conformation and dynamics. *Proc. Natl Acad. Sci. USA* **78**, 2179–2183 (1981).
101. Müller, J., Oehler, S. & Müller-Hill, B. Repression of lac promoter as a function of distance, phase and quality of an auxiliary lac operator. *J. Mol. Biol.* **257**, 21–29 (1996).
102. Hochschild, A. & Ptashne, M. Cooperative binding of lambda repressors to sites separated by integral turns of the DNA helix. *Cell* **44**, 681–687 (1986).
103. Ghosh, R. P. et al. Satb1 integrates DNA binding site geometry and torsional stress to differentially target nucleosome-dense regions. *Nat. Commun.* **10**, 3221 (2019).
104. Zhu, F. et al. The interaction landscape between transcription factors and the nucleosome. *Nature* **562**, 76–81 (2018).
105. Ptashne, M. Regulation of transcription: from lambda to eukaryotes. *Trends Biochem. Sci* **30**, 275–279 (2005).
106. Sun, Y. et al. Zelda overcomes the high intrinsic nucleosome barrier at enhancers during *Drosophila* zygotic genome activation. *Genome Res.* **25**, 1703–1714 (2015).
107. Thanos, D. & Maniatis, T. Virus induction of human IFNβ gene expression requires the assembly of an enhanceosome. *Cell* **83**, 1091–1100 (1995).
108. Merika, M. & Thanos, D. Enhanceosomes. *Curr. Opin. Genet. Dev.* **11**, 205–208 (2001).
109. Li, Q. & Wrange, O. Accessibility of a glucocorticoid response element in a nucleosome depends on its rotational positioning. *Mol. Cell. Biol.* **15**, 4375–4384 (1995).
110. Sharon, E. et al. Inferring gene regulatory logic from high-throughput measurements of thousands of systematically designed promoters. *Nat. Biotechnol.* **30**, 521–530 (2012).
111. Cai, H. N., Arnosti, D. N. & Levine, M. Long-range repression in the *Drosophila* embryo. *Proc. Natl Acad. Sci. USA* **93**, 9309–9314 (1996).
112. Cui, F. & Zhurkin, V. B. Rotational positioning of nucleosomes facilitates selective binding of p53 to response elements associated with cell cycle arrest. *Nucleic Acids Res.* **42**, 836–847 (2014).
113. Suryamohan, K. & Halfon, M. S. Identifying transcriptional cis-regulatory modules in animal genomes. *Wiley Interdiscip. Rev. Dev. Biol.* **4**, 59–84 (2015).
114. Istrail, S. Eric Davidson's regulatory genome for computer science: causality, logic, and proof principles of the genomic cis-regulatory code. *J. Comput. Biol.* **26**, 653–684 (2019).
115. Slattery, M. et al. Absence of a simple code: how transcription factors read the genome. *Trends Biochem. Sci.* **39**, 381–399 (2014).
116. Tseng, A. M., Shrikumar, A. & Kundaje, A. Fourier-transform-based attribution priors improve the interpretability and stability of deep learning models for genomics. Preprint at *bioRxiv* https://doi.org/10.1101/2020.06.11.147272 (2020).
117. Klemenz, R., Stillman, D. J. & Geiduschek, E. P. Specific interactions of *Saccharomyces cerevisiae* proteins with a promoter region of eukaryotic tRNA genes. *Proc. Natl Acad. Sci. USA* **79**, 6191–6195 (1982).
118. Oler, A. J. et al. Human RNA polymerase III transcriptomes and relationships to Pol II promoter chromatin and enhancer-binding factors. *Nat. Struct. Mol. Biol.* **17**, 620–628 (2010).

Methods

Cell culture. R1 ESCs were cultured on 0.1% gelatin-coated plates without feeder cells in N2B27 medium (DMEM/F12 with 1:1 mix of GlutaMax/N2 and Neurobasal medium/B27, Invitrogen) supplemented with 2 mM L-glutamine (Stemcell Technologies), 1× 2-mercaptoethanol (Millipore), 1× NEAA (Stemcell Technologies), 3 µM CHIR99021 (Stemcell Technologies), 1 µM PD0325901 (Stemcell Technologies), 0.033% BSA solution (Invitrogen) and 10^7 U ml^{-1} LIF (Millipore).

ChIP–nexus, PATCH–CAP and ChIP–seq experiments. For each ChIP–nexus experiment, 10 million ESCs were used. Cells were washed with PBS and cross-linked with 1% formaldehyde (Fisher Scientific) in PBS for 10 min at room temperature. The reaction was quenched with 125 mM glycine. Fixed cells were washed twice with cold PBS, resuspended in cold lysis buffer (15 mM HEPES pH 7.5, 140 mM NaCl, 1 mM EDTA, 0.5 mM EGTA, 1% Triton X-100, 0.5% *N*-lauroylsarcosine, 0.1% sodium deoxycholate and 0.1% SDS), incubated for 10 min on ice and sonicated with a Bioruptor Pico (Diagenode) for five cycles of 30 s on and 30 s off. The ChIP–nexus procedure and data processing were performed as previously described[49], except that the ChIP–nexus adapter mix contained four fixed barcodes (ACTG, CTGA, GACT and TGAC) and PCR library amplification was performed directly after circularization of the purified DNA fragments (without addition of the oligo and BamHI digestion). PATCH–CAP was performed as previously described[59] with 10% of sheared chromatin from 10 million ESCs. ChIP–seq experiments were performed as previously described[119] with 10 million ESCs per ChIP.

For each ChIP, 5 µg of antibody was coupled to 50 µl of Protein A or Protein G Dynabeads (Invitrogen). The following antibodies were used: anti-Oct3/4 (Santa Cruz, no. sc-8628), anti-Sox2 (Santa Cruz, no. sc-17320), anti-Sox2 (Active Motif, no. 39843), anti-Nanog (Santa Cruz, no. sc-30328), anti-Klf4 (R&D Systems, no. AF3158), anti-Klf4 (Abcam, no. ab106629), anti-Esrrb (Abcam, no. ab19331), anti-Pbx 1/2/3 (Santa Cruz, no. sc-888) and anti-Zic3 (Abcam, no. ab222124). For all experiments, at least two biological replicates were prepared—that is, the experiments were performed on different days starting with cells from a different passage number. Single-end sequencing was performed on either an Illumina HiSeq (50 cycles) or NextSeq 500 instrument (75 cycles).

Mutation of binding motifs using CRISPR/Cas9 technology. Using mouse R1 ESCs, the predicted *Nanog* motif on chr10: 85,539,756–85,539,765 (mm10) was mutated from C**TGA**TGGCT (wild type) to C**GGC**TGGCT (mutant). The predicted *Sox2* motif on chr10: 85,539,634–85,539,643 (mm10) was mutated from CCT**TT**GTTCC (wild type) to CCT**AG**GTTCC (mutant). Guide RNA target sites were designed using the CCTop target predictor tool[120] by evaluation of the predicted on-target efficiency score and off-target potential[121]. The single-stranded donor oligonucleotides (ssODN) were designed containing ~40 bases of homology from the targeted cut site (gRNA and ssODN sequences are shown in Supplementary Table 3). A ribonucleoprotein (RNP) complex was formed by combining 90 pmol of gRNA (ordered as Alt-R single-guide RNA; IDT) and 10 pmol of Cas9 HiFi protein (IDT) with hybridization for 10 min at room temperature. The RNP was combined with 100 pmol of ssODN donor and delivered to cells by Neon electroporation (1,500 V, 10 ms, three pulses; Neon Transfection System, Model MPK5000, Life Technologies). Single cells were screened for the expected mutations through paired-end sequencing on an Illumina MiSeq instrument (250 cycles). On-target indel frequency and expected mutations were analyzed using CRIS.py[122]. Only clones with the intentional mutation and sequence alignments >90% were chosen for future experiments.

Per target site, three monoclonal cell lines were selected and used as replicate experiments: clones B07, B09 and F10 for the mutant *Nanog* motif, and clones B07, B11 and C10 for the mutant *Sox2* motif. For the wild-type R1 ESC control samples, at least two biological replicates were prepared as above. ChIP–nexus was performed as described above (ChIP–nexus, PATCH–CAP and ChIP–seq experiments) with 20 million ESCs and 5 µg of anti-Nanog (Abcam, no. ab214549) or anti-Sox2 (Active Motif, no. 39843) per replicate. The following fixed barcodes were used: AGTC, CAGT, GTCA and TCAG. Single-end sequencing was performed on an Illumina NovaSeq instrument (100 cycles) to obtain a coverage of ~400 million reads per experiment.

ChIP–nexus data processing pipeline. Random barcodes and fixed barcodes were trimmed off the reads and reassigned to FASTQ labels using nimnexus (v.0.1.1). The adapters were then trimmed using cutadapt (v.1.8.1)[123]. Next, the reads were aligned with Bowtie (v.1.1.12)[124,125] using the command bowtie --chunkmbs 512 -k 1 -m 1 -v 2 --best --strata to the mouse genome assembly mm10. Mutant samples were aligned to a modified mm10 genome that accommodated the CRISPR changes. Mapping statistics were computed using SAMtools flagstat (v.1.2)[126]. Reads were filtered using SAMtools view to remove unmapped reads and mates, nonprimary alignments, PCR or optical duplicates (-F 1804) and reads that failed platform or vendor quality checks or had poor mapping quality (<30 MAPQ score). Reads aligned to the same position with the same barcode, CIGAR string and the SAM flag were deduplicated using nimnexus dedup (v.0.1.1). The total number of final (filtered) aligned reads was 243 million for Oct4, 140 million for Sox2, 214 million for Nanog and 176 million for Klf4. The final filtered BAM file was converted to tagAlign format (BED 3+3) using bedtools 'bamtobed' (v.2.26)[127]. Cross-correlation scores were obtained for each file using phantompeakqualtools (v.1.2)[128]. BigWig tracks containing the strand-specific number of aligned 5′ read ends (pooled across all replicates) were generated using bedtools genomecov -5 -bg –strand <+/–>, followed by bedGraph to BigWig conversion using UCSC bedGraphToBigWig v.4 (ref. [129]).

Peaks were called using MACS2 (v.2.1.1.20160309) by extending the 5′ ends of reads on each strand using a 150-bp window (±75 bp) and then computing coverage of extended reads across both strands (shift = −75, extsize = 150). For each TF, peak calling was performed on filtered, aligned reads from each replicate using a relaxed *P* threshold of 0.1 and retaining the top 300,000 peaks as described[128]. Relaxed peak calls were similarly performed on pseudoreplicates, which were obtained by pooling filtered, aligned reads from all replicates for a TF and randomly splitting the pooled reads into two balanced pseudoreplicates. Peaks overlaping the blacklisted regions listed in https://www.encodeproject.org/files/ENCFF547MET/ were excluded. The irreproducible discovery rate (IDR) framework was used to obtain reproducible peaks across the true replicates and pseudoreplicates[130]. The set with the larger number of peaks was defined as the IDR optimal peaks for each TF: 25,849 for Oct4, 10,999 for Sox2, 56,459 for Nanog and 57,601 for Klf4. Regions of 1 kb centered on the peak summits were used as inputs to BPNet. All samples passed quality control metrics used in the ENCODE TF ChIP–seq pipeline[128] (Supplementary Table 1).

The nim-nexus code is available at https://github.com/Avsecz/nimnexus/. The ChIP–nexus pipeline performing the described steps (for example, turning raw reads in FASTQ format to BigWig coverage tracks and called peaks) is available at https://github.com/kundajelab/chip-nexus-pipeline. A detailed pipeline specification is available at https://docs.google.com/document/d/1h9lZ0GyVWd02RCmtaFWSaSFzrcNHoH_OgyPHMpU7b04. ChIP–seq datasets were processed using the ENCODE ChIP–seq pipeline: https://github.com/ENCODE-DCC/chip-seq-pipeline2/releases/tag/v1.2.2. This is identical to the ChIP–nexus pipeline except that it uses the SPP peak caller[29] and does not use barcodes for read deduplication.

BPNet architecture. BPNet is a sequence-to-profile convolutional neural network that uses one-hot-encoded DNA sequence (A = [1,0,0,0], C = [0,1,0,0], G = [0,0,1,0], T = [0,0,0,1]) with adjustable length as input to predict base-resolution read count profiles as output. For flexibility, the architecture of BPNet can be compartmentalized into body- and multiple task-specific output heads. The body of BPNet consists of a sequence of convolutional layers with residual skip connections and rectified linear activations[57]. The first convolutional layer uses 64 filters of width 25 bp, followed by nine dilated convolutional layers (each with 64 filters of width 3) where the dilation rate (number of skipped positions in the convolutional filter) doubles at every layer. This results in a receptive field of ±1,034 bp for any position in the input sequence. The output of the final convolutional layer within the BPNet body (also referred to as the bottleneck activation map) serves as input for two output heads per TF: (1) a deconvolutional layer (filter width 25—a typical ChIP–nexus footprint width) predicting the strand-specific probabilities of observing a particular read at a particular position in the input sequence (shape or profile prediction); and (2) a global average pooling layer followed by the fully connected layer predicting the total number of read counts aligned to the input sequence for each strand (total read count prediction). The training occurs for all TF ChIP–nexus experiments together in a multitask fashion. BPNet architecture (without bias correction) implementation in Keras v.2.2.4 is provided in Supplementary Methods.

BPNet loss function. Let $\mathbf{k}^{\text{obs}}$ be the vector of length L of observed read counts for a particular strand and a particular task (that is, TF) along the sequence of length L. Let $\mathbf{p}^{\text{pred}}$ be the vector of length L of predicted probabilities along the sequence, such that $\sum p_i = 1$ and let $n^{\text{obs}} = \sum k_i^{\text{obs}}$ be the total number of observed counts and n^{pred} the total number of predicted counts for the sequence. The following loss function is used for each sequence, strand and task:

$$\text{Loss} = -\log \mathbf{p}_{\text{mult.}}\left(\mathbf{k}^{\text{obs}} | \mathbf{p}^{\text{pred}}, n^{\text{obs}}\right) + \lambda\left(\log\left(1+n^{\text{obs}}\right) - \log\left(1+n^{\text{pred}}\right)\right)^2.$$

The first term evaluates the error in the shape of the predicted profile. It is the multinomial $\left(\mathbf{p}_{\text{mult.}}(\mathbf{k}|\mathbf{p},\mathbf{n}) = \frac{n!}{k_1!\cdots k_d!} p_1^{k_1}\cdots p_d^{k_d}\right)$ negative log-likelihood of observed base read counts given the predicted probabilities and total number of observed counts. The second term evaluates the squared error of the log total number of reads in the region. During BPNet training, the total loss function is the sum of individual loss functions across both strands, all input sequences and all tasks.

The key hyperparameter is λ. In Supplementary Methods (relationship between Poisson log-likelihood, mean-squared error and multinomial log-likelihood), we show that if $\lambda = \bar{n}^{\text{obs}}/2$, where $\bar{n}^{\text{obs}}$ is the average number of total counts across all sequences in our training set, profile loss and total count loss will be given roughly equal weight. To upweight the profile predictions relative to the total count predictions, $\lambda = \frac{\alpha}{2} n^{\text{obs}}$ with $\alpha < 1$ can be used.ð

Control for biases by BPNet. Experimental assays often have biases that can be measured by control experiments (input for ChIP–seq and PATCH–CAP for ChIP–nexus[59]). To prevent the sequence-to-profile model from learning these noninformative bias signals, the model tries to explain the target experimental track (for example, the Oct4 profile) using both the sequence-based model predictions $\mathbf{f}^h_{\text{model}}(\text{seq}; \mathbf{w}^h)$for specific head h and the control experiment track, ctl:

$$\mathbf{y}^h_{\text{pred}} = \mathbf{f}^h_{\text{model}}(\text{seq}; \mathbf{w}^h) + \mathbf{f}^h_{\text{ctl}}(\text{ctl}; \mathbf{w}^h_{\text{ctl}}) \ ,$$

where $\mathbf{f}^h_{\text{ctl}}(\text{ctl}; \mathbf{w}^h_{\text{ctl}})$ is a neural network-based transformation of the control track aimed at explaining data for head h. Integration with the control data therefore occurs after the task-specific model head $\mathbf{f}^h_{\text{model}}$. We require that $\mathbf{f}^h_{\text{ctl}}(\text{ctl}; \mathbf{w}^h_{\text{ctl}}) = 0$ if the control track is 0 (that is, bias not present) so that the model $\mathbf{f}^h_{\text{model}}$ represents the bias-free part of the signal. Each head/track will have a different bias transformation either by having different parameters, $\mathbf{w}^h_{\text{ctl}}$, or even a different architecture for $\mathbf{f}^h_{\text{ctl}}$. For the total count prediction head, $\mathbf{f}^h_{\text{ctl}}(\text{ctl}; \mathbf{w}^h_{\text{ctl}})$ is simply $\mathbf{w}^h_{\text{ctl}} \log(1 + n_{\text{ctl}})$, where n_{ctl} is the total number of reads from the control experiment in the modeled local region. For the profile prediction head, $\mathbf{f}^h_{\text{ctl}}(\text{ctl}; \mathbf{w}^h_{\text{ctl}})$is a weighted sum of (1) the raw counts and (2) a smoothed version of the raw counts using a sliding window sum of 50 bp (since control data are often sparse). During model training, the parameters of $\mathbf{f}^h_{\text{ctl}}(\text{ctl}; \mathbf{w}^h_{\text{ctl}})$ are also trained to best explain the output using the control track. This framework readily integrates multiple control tracks, or control tracks predicted from sequence, using a bias model learned on other data such as deproteinized genomic DNA for DNase-seq[131].

BPNet training and hyperparameter tuning. ChIP–nexus profiles of Oct4, Sox2, Nanog and Klf4 were used to train and evaluate BPNet. Regions from mouse chromosomes 2, 3 and 4 (20%) were used as the tuning set for hyperparameter tuning. Regions from chromosomes 1, 8 and 9 (20%) were used as the test set for performance evaluation (Supplementary Methods). The remaining regions were used for model training. Hyperparameters were manually adjusted to yield best performance on the tuning set. All neural network models were implemented and trained in Keras (v.2.2.4)[132] (TensorFlow backend v.1.6) using the Adam optimizer[133] (learning rate = 0.004) and early stopping with patience of five epochs.

DeepLIFT contribution scores for sequence-to-profile models. DeepLIFT is a feature attribution method for computing the contribution of each base (feature) in an input sequence to a specific scalar output prediction from a neural network model[65]. DeepLIFT decomposes the difference between the output prediction from an input sequence versus that of a neutral reference input sequence as an additive combination of contribution scores of all bases (D features) in the input sequence:

$$\mathbf{f}(\mathbf{x}) - \mathbf{f}(\mathbf{r}) = \sum_i^D c_i$$

where c_i is the contribution of feature i in input $\mathbf{x}$ to the model output prediction $\mathbf{f}(\mathbf{x})$ compared to model prediction $\mathbf{f}(\mathbf{r})$ based on the reference input $\mathbf{r}$.

The output of BPNet for each head is, however, not a scalar, but a *2D* tensor of size $L \times S$, where L is the sequence length and S is the number of output channels or strands for ChIP–nexus. We therefore needed to adapt DeepLIFT and defined the profile contribution score of a base with respect to the entire output profile as follows:

$$c^{(\text{profile})} = \sum_{i,s} c_{is} P_{is}$$

where P_{is} is the predicted probability values for position i and strand s, obtained by normalizing the profile predictions on the logit scale using the softmax function along the sequence axis: $\mathbf{p} = \text{softmax}(\mathbf{f}(\mathbf{x}))$. c_{is} is the contribution score of the base with respect to the (scalar) profile prediction on the logit scale at position i and strand s. A weighted sum is used to ensure that positions with high predicted profile output values are given more weight, but has the disadvantage that it would normally require the contribution scores to be computed $L \times S$ (2,000) times for each 1-kb input sequence per TF. To drastically accelerate this computation, we exploit the backpropagation algorithm used in DeepLIFT and the additive decomposition of DeepLIFT scores. We define a new TensorFlow operation as follows:

$$\hat{f}(\mathbf{x}) = \sum_i \text{Const}\big(p_i(\mathbf{x})\big) f_i(\mathbf{x}),$$

where Const denotes the tf.stop_gradients operation, which treats the wrapped expression $p_i(\mathbf{x})$ as a constant. By applying DeepLIFT to $\hat{f}(\mathbf{x})$, we obtain the desired result in a single DeepLIFT backpropagation step:

$$c^{(\text{profile})} = \sum_{i,s} c_{is} p_{is}.$$

Pseudocode of the described operation in TensorFlow code is:

```
wn = tf.reduce_mean(tf.reduce_sum(tf.stop_gradient(tf.
nn.softmax(f, dim=-2)) * f, axis=-2), axis=-1).
```

For the reference input $\mathbf{r}$, all zeroes were used since it showed the highest correlation with in silico mutagenesis contribution scores, defined as the weighted sum of the profile prediction changes at all profile locations after introduction of a mutation at a particular position. The DeepLIFT contribution scores were computed with TensorFlow v.1.6 using the DeepExplain implementation of DeepLIFT (repository fork available at https://github.com/kundajelab/DeepExplain/, with commit hash: 738c7145e915a7a48f3a4248d088bcc2e1a94614).

Motif discovery using TF–Modisco. TF–Modisco (v.0.5.1.1) was run on DeepLIFT profile contribution scores for each TF separately (using all 1-kb peak regions bound by the TF on autosomes). Significant seqlets were selected by computing contribution scores over a width of 21 bp and using the false-discovery rate threshold of 0.01 (target_seqlet_fdr). The null distribution was estimated from 4,800 randomly selected peaks with contribution scores computed on reshuffled sequences while preserving dinucleotide counts. A total of 145,748 nonoverlapping significant seqlets were identified. Due to memory constraints (250 GB), 50,000 seqlets were used for each TF during the clustering/motif-discovery phase of TF–Modisco. For all discovered motifs, PFM and CWM are computed from the aligned seqlets by averaging the base frequencies and contribution scores, respectively (Supplementary Methods).

Clustering of discovered motifs. Motifs were aligned to each other in all possible offsets and strand combinations, and a pairwise distance metric was generated using the smallest continuous Jaccard distance metric[41] on the PFM information content between each motif pair. Hierarchical clustering was performed in scipy (v.1.2.1) using the Ward variance minimization algorithm[134] (method='ward') and optimal leaf ordering[135] (Extended Data Fig. 2d). From these clusters, 11 representative TF motifs were manually selected.

Identification of motif instances by CWM scanning. Once BPNet is trained it is possible, but not necessary, to use the experimentally measured ChIP–nexus profiles during model interpretation. For the mapping of motifs with TF–Modisco and CWM scanning, no information from the experimental profiles was used. CWM scanning was developed because TF–Modisco analyzes only 50,000 seqlets per run. Trimmed CWMs were used to scan the contribution scores of all 147,974 peak regions (as done by TF–Modisco) and by computing the following similarity metric. Let $\mathbf{w}^{\text{CWM}} \in \mathbb{R}^{L_W \times 4}$ denote the CWM of length L_W and $\mathbf{C} \in \mathbb{R}^{L_S \times 4}$ denote the contribution scores for one-hot-encoded sequence s of length $L_S \geq L_W$. The contribution score $C_{i,b}$ for base b at position i is 0 if base b was not observed in the actual sequence (that is, if $s_{i,b} = 0$). We decompose the similarity metric between the CWM scanning position i of the contribution scores into the 'contrib' score, computed as the L1 norm of the contribution scores at positions between i and $i + L_W$ in the scanned sequence:

$$\text{Score}_{\text{contrib}}\left(\mathbf{w}^{\text{CWM}}, \mathbf{C}, i\right) = \sum_{j=1}^{L_W} \sum_{b=1}^{4} \left| C_{i+j-1,b} \right| \ ,$$

and the 'match' score, which represents its similarity to the CWM computed using the continuous Jaccard distance metric[41] between the CWM and L1-normalized contribution scores:

$$\text{Score}_{\text{match}}\left(\mathbf{w}^{\text{CWM}}, \mathbf{C}, i\right) = \text{Jaccard}\left(\frac{\mathbf{w}^{\text{CWM}}}{||\mathbf{w}^{\text{CWM}}||_1}, \frac{\mathbf{C}_{i:i+L_W,b}}{||\mathbf{C}_{i:i+L_W,b}||_1}\right),$$

At each position i, the maximum 'match' score ($\text{Score}_{\text{match}}$) between $\mathbf{w}^{\text{CWM}}$ and its reverse-complement version is chosen. To call motif instances from the CWM scanning scores, three criteria were defined based on thresholds identified from the TF–Modisco corresponding seqlets: (1) The match score >20th percentile of those of the seqlets. This stringent threshold more effectively discriminates between similar motifs. (2) The contrib score is higher than the seqlets lowest contrib score. (3) The log odds score with respect to the PWM derived from the PFM is >0.

In silico motif interaction analysis. In the synthetic approach, two consensus motifs were inserted into 128 random background sequences of 1 kb: *Motif A* at the center and *Motif B* downstream at distance d between the motif centers (maximum at 160 bp). The average strand-specific ChIP–nexus profile predictions, P_{AB}, for the TF that binds *Motif A* were then obtained using the trained BPNet model as oracle. Additional profiles were predicted by (1) inserting only *Motif A* in the center (P_{A}), (2) inserting only *Motif B* d-bases downstream of the center (P_{B}) and (3) not inserting any motif ($P_{\emptyset}$). The strand-specific summit (maximum) location of the footprint was then determined for each strand from profile P_{A} within 35 bp of the *Motif A* center. These summit locations were used to determine the footprint height, h, within all four profiles to obtain h_{A}, h_{B}, h_{AB} and $h_{\emptyset}$. The influence of *Motif B* on *Motif A* was then defined by the corrected binding fold change $(h_{\text{AB}} - (h_{\text{B}} - h_{\emptyset}))/h_{\text{A}}$ as a function of d. The procedure was repeated to quantify the influence of *Motif A* on the binding of TF B to *Motif B*. In the genomic motif interaction approach, motif pair interactions were calculated in the same way using motif instances that were mapped by CWM scanning in genomic sequences underlying ChIP–nexus peaks, excluding motif instances overlapping

retrotransposons. Rather than inserting motifs into the random sequence, motifs were removed from the genomic sequence by replacing them with random sequences (Supplementary Methods and Supplementary Fig. 10).

Reproducibility. All ChIP–nexus and ChIP–seq replicate experiments passed quality control metrics used by ENCODE[128] (Supplementary Table 1). For Sox2 and Nanog, we used two different antibodies for each with reproducible results: the initial wild-type Sox2 ChIP–nexus experiments used two different antibodies (sc-17320 and Active Motif 39843) with IDR rescue ratio < 2; the wild-type and CRISPR Nanog ChIP–nexus experiments also used two different antibodies (sc-30328 and ab-214549) with consistent Nanog footprints on *Nanog* motifs (Extended Data Fig. 3). The entire pipeline, including the training of BPNet, computation of contribution scores, obtaining motif representations and analysis of motif interactions, was performed in fivefold cross-validation, which supports our claims (Supplementary Information and Supplementary Figs. 4, 11 and 12). The CRISPR mutant and wild-type experiments were consistent in both profile and counts at control enhancers (Extended Data Fig. 8), and replicate experiments were highly reproducible (Supplementary Fig. 14).

Reporting Summary. Further information on research design is available in the Nature Research Reporting Summary linked to this article.

Data availability

The raw sequencing data are available from GEO under accession number GSE137193. Data used to train, evaluate and interpret the BPNet models are found on zenodo at https://doi.org/10.5281/zenodo.3371215. Trained BPNet models and all the model interpretation results are on zenodo at https://doi.org/10.5281/zenodo.3371163. The BPNet model trained on ChIP–nexus data is available on Kipoi under the name BPNet-OSKN (http://kipoi.org/models/BPNet-OSKN/). Genome browser tracks showing observed/predicted ChIP–nexus signal and contribution scores for all factors are available at https://genome.ucsc.edu/s/mlweilert/mesc_OSKN_tracks. ATAC-seq data in mouse ESCs used in Fig. 2 and Supplementary Fig. 7 were obtained from GSE134680. Blacklisted regions used to filter genomic coordinates throughout the analysis are available at https://www.encodeproject.org/files/ENCFF547MET. RepeatMasker mm10 annotations were obtained from http://www.repeatmasker.org/genomes/mm10/RepeatMasker-rm405-db20140131/mm10.fa.out.gz. The nuclear magnetic resonance structure 1O4X used to render Sox2 and Oct1 in Fig. 3 is available at https://www.rcsb.org/structure/1o4x. TRANSFAC (v.7.0) was used to identify the TFIIIC B-box discussed in Fig. 3. The PH0134.1 Pbx PWM used for motif validation in Supplementary Fig. 8 and Extended Data Fig. 5 was obtained from JASPAR at http://jaspar.genereg.net/api/v1/matrix/PH0134.1.jaspar. The MA0141.1 Esrrb PWM used in Extended Data Fig. 5 was obtained from JASPAR at http://jaspar.genereg.net/api/v1/matrix/MA0141.1.jaspar. The transfer RNA database GtRNAdb (v.2.0, release 17.1) annotations and associated tRNAscan-SE scores used in Extended Data Fig. 5 were obtained from http://gtrnadb.ucsc.edu/GtRNAdb_archives/release17/genomes/eukaryota/Mmusc10/mm10-tRNAs.tar.gz. Source data are provided with this paper.

Code availability

The BPNet software package is available at https://github.com/kundajelab/bpnet/. Code to reproduce the results is available at https://github.com/kundajelab/bpnet-manuscript (https://doi.org/10.5281/zenodo.4294813). The ChIP–nexus data processing pipeline is available at https://github.com/kundajelab/chip-nexus-pipeline. Software to trim and deduplicate ChIP–nexus reads is available at https://github.com/Avsecz/nimnexus/.

References

119. Koenecke, N., Johnston, J., He, Q., Meier, S. & Zeitlinger, J. *Drosophila* poised enhancers are generated during tissue patterning with the help of repression. *Genome Res.* **27**, 64–74 (2017).
120. Stemmer, M., Thumberger, T., Del Sol Keyer, M., Wittbrodt, J. & Mateo, J. L. Cctop: an intuitive, flexible and reliable crispr/cas9 target prediction tool. *PLoS ONE* **10**, e0124633 (2015).
121. Labuhn, M. et al. Refined sgRNA efficacy prediction improves large- and small-scale CRISPR-Cas9 applications. *Nucleic Acids Res.* **46**, 1375–1385 (2018).
122. Connelly, J. P. & Pruett-Miller, S. M. CRIS.py: a versatile and high-throughput analysis program for CRISPR-based genome editing. *Sci. Rep.* **9**, 4194 (2019).
123. Martin, M. Cutadapt removes adapter sequences from high-throughput sequencing reads. *EMBnet J.* **17**, 10 (2011).
124. Li, H. & Durbin, R. Fast and accurate short read alignment with Burrows–Wheeler transform. *Bioinformatics* **25**, 1754–1760 (2009).
125. Langmead, B., Trapnell, C., Pop, M. & Salzberg, S. L. Ultrafast and memory-efficient alignment of short DNA sequences to the human genome. *Genome Biol.* **10**, R25 (2009).
126. Li, H. et al. The Sequence Alignment/Map format and SAMtools. *Bioinformatics* **25**, 2078–2079 (2009).
127. Quinlan, A. R. & Hall, I. M. BEDTools: a flexible suite of utilities for comparing genomic features. *Bioinformatics* **26**, 841–842 (2010).
128. Landt, S. G. et al. ChIP–seq guidelines and practices of the ENCODE and modENCODE consortia. *Genome Res.* **22**, 1813–1831 (2012).
129. Kent, W. J., Zweig, A. S., Barber, G., Hinrichs, A. S. & Karolchik, D. BigWig and BigBed: enabling browsing of large distributed datasets. *Bioinformatics* **26**, 2204–2207 (2010).
130. Li, Q., Brown, J. B., Huang, H. & Bickel, P. J. Measuring reproducibility of high-throughput experiments. *Ann. Appl. Stat.* **5**, 1752–1779 (2011).
131. Yardımcı, G. G., Frank, C. L., Crawford, G. E. & Ohler, U. Explicit DNase sequence bias modeling enables high-resolution transcription factor footprint detection. *Nucleic Acids Res.* **42**, 11865–11878 (2014).
132. Chollet, F. et al. Keras. https://keras.io (2015).
133. Kingma, D. P. & Ba, J. Adam: a method for stochastic optimization. *dblp: Computer Science Bibliography* https://dblp.org/rec/journals/corr/KingmaB14.html (2015).
134. Ward, J. H. Hierarchical grouping to optimize an objective function. *J. Am. Stat. Assoc.* **58**, 236–244 (1963).
135. Bar-Joseph, Z., Gifford, D. K. & Jaakkola, T. S. Fast optimal leaf ordering for hierarchical clustering. *Bioinformatics* **17**, S22–S29 (2001).

Acknowledgements

We thank M. Levine and R. Krumlauf for comments and J. Israeli for initial technical help. This work was funded by the Stowers Institute for Medical Research (SIMR), NIH grant no. R01HG010211 to J.Z. and NIH grant nos. DP2GM123485, U01HG009431 and R01HG009674 to A.K. Ž.A. was supported by the German Bundesministerium für Bildung und Forschung through the project MechML (no. 01IS18053F). A.S. was supported by the Stanford BioX Fellowship and HHMI International Student Research Fellowship. Illumina sequencing was performed at SIMR (A. Perera and M. Peterson) and the University of Kansas Medical Center Genomics Core, supported by NIH grant nos. U54HD090216, S10OD021743 and COBRE P30GM122731. Generation of CRISPR/Cas9 mouse ESC lines was performed by the following cores at SIMR: Genome Engineering (K. Delventhal, B. Miller and K. Weaver), Tissue Culture (C. Zhao, A. Murray, Y. Wang, O. Kenzior, Q. Jiang, S. Hime and S. Gosh) and Cytometry (J. Haug and D. DeGraffenreid).

Author contributions

Ž.A., A.K. and J.Z. conceived the project. Ž.A., A.S., A.K. and J.Z. conceived and implemented the computational methods. S.K., K.D. and R.F. performed the experiments. Ž.A., M.W., A.A. and C.M. performed further computational analysis. J.Z., A.K. and J.G. supervised the project. Ž.A., M.W., S.K., J.G., A.K. and J.Z. prepared the manuscript with input from all authors.

Competing interests

J.Z. owns a patent on ChIP–nexus (no. 10287628). All other authors declare no competing interests.

Additional information

Extended data is available for this paper at https://doi.org/10.1038/s41588-021-00782-6.

Supplementary information The online version contains supplementary material available at https://doi.org/10.1038/s41588-021-00782-6.

Correspondence and requests for materials should be addressed to A.K. or J.Z.

Peer review information *Nature Genetics* thanks the anonymous reviewers for their contribution to the peer review of this work. Peer reviewer reports are available.

Reprints and permissions information is available at www.nature.com/reprints.

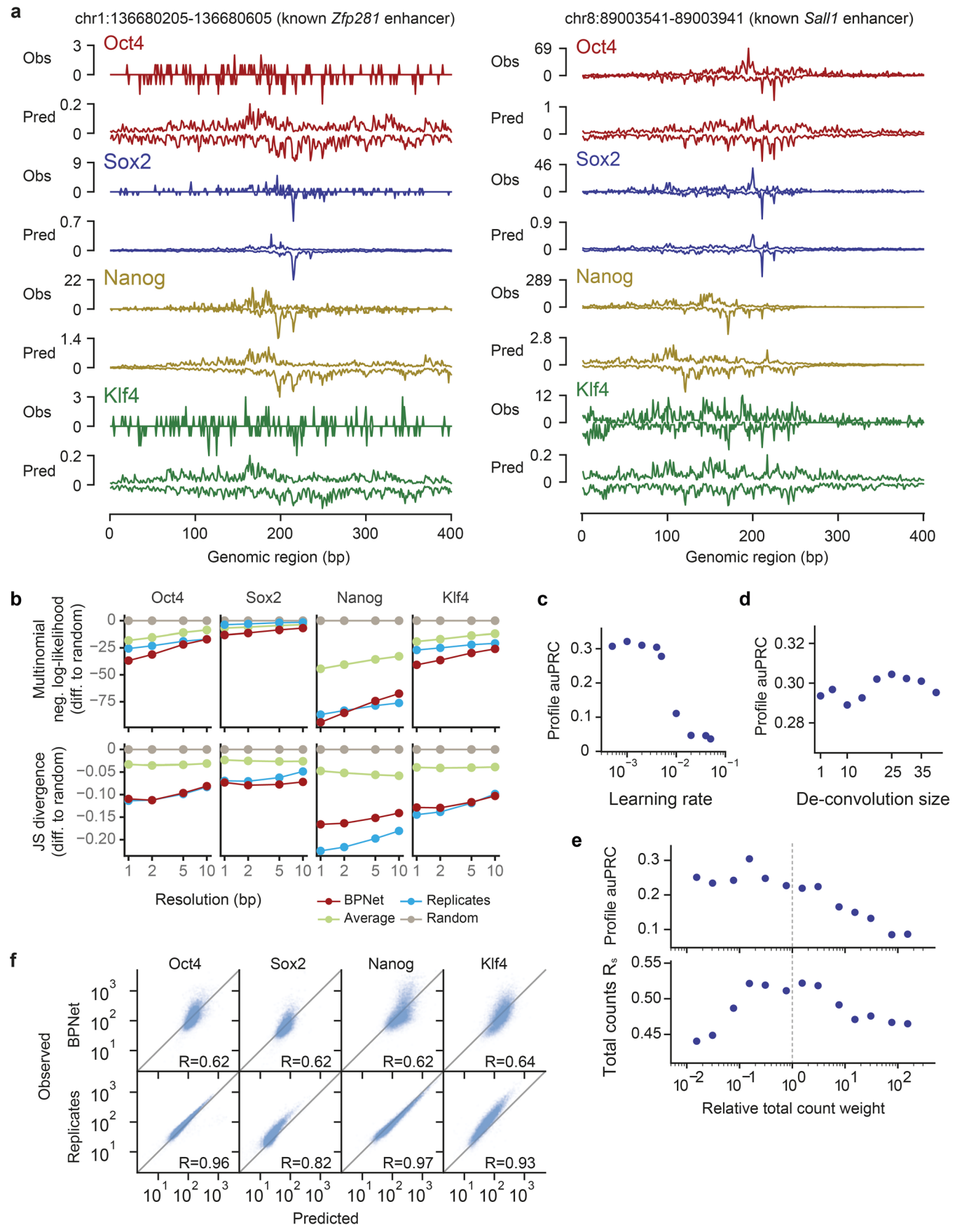

Extended Data Fig. 1 | See next page for caption.

Extended Data Fig. 1 | Additional performance evaluation of BPNet's predictions of ChIP-nexus data. a, Observed and predicted ChIP-nexus read counts mapping to the forward strand (dark) and the reverse strand (light) for the *Zfp281* and *Sall1* enhancers located on the held-out (test) chromosome 1. **b,** Alternative profile shape evaluation metrics showing the difference to random predictions: multinomial negative log-likelihood and Jensen-Shannon (JS) divergence. Both metrics were computed at different resolutions (from 1 bp to 10 bp windows) in held-out test chromosomes 1, 8 and 9. **c,** auPRC of profile predictions is high across various learning rates on the tuning set chromosomes 2, 3 and 4, demonstrating the robustness of the model. **d,** The deconvolutional layer slightly improves the profile predictive performance compared to a point-wise convolutional layer (deconvolution size=1). **e,** auPRC of profile predictions (top) and the Spearman correlation of total count predictions (bottom) for a range of different relative total count weight α in the BPNet loss function parameterized as $\lambda = \alpha/2$ n_obs. Relative weight of 1 (center) denotes equal weighting of the counts and profile loss functions. The best performance is obtained for $\alpha<1$, showing that putting more weight to profile predictions aids both profile and count predictions. **f,** Observed and predicted total read counts for BPNet (top) and replicate experiments (bottom) across the four studied TFs along with the Spearman correlation coefficient.

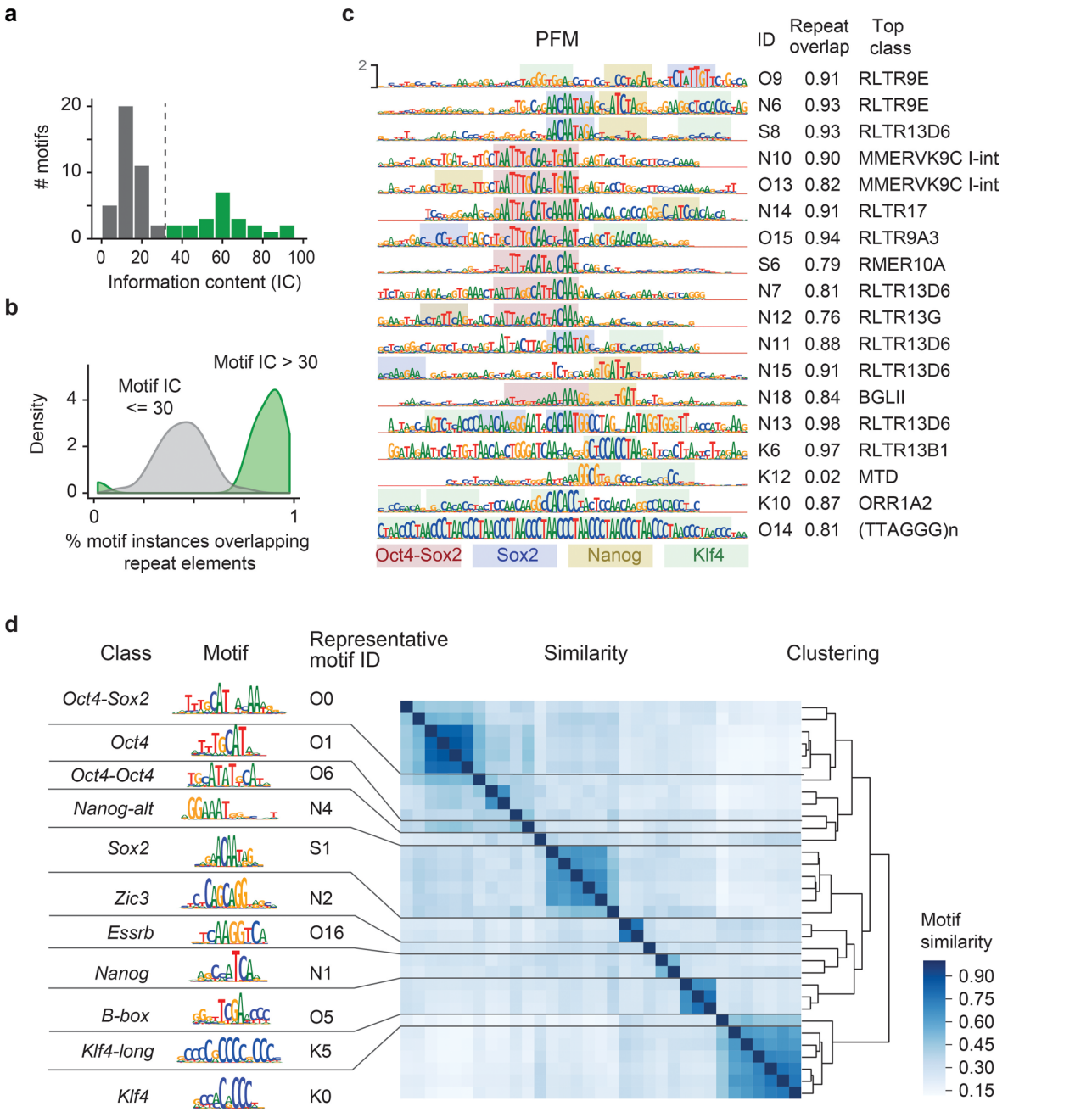

Extended Data Fig. 2 | Removal of long motifs in retrotransposons and clustering of motifs by similarity. a, Among all motifs discovered by TF-MoDISco, 18 motifs display unusually high information content (IC) of >30 bits (green). The expected short motifs are shown in gray. **b,** Histogram of the overlap of short motifs (gray) and long motifs (green) with repeat elements shows that long motifs overlap >80% with annotated retrotransposons. **c,** Long motifs with their PFM, ID, fraction of motif instances overlapping with a repeat and the most frequent (top class) RepeatMasker annotation. Highlighted within the repeat elements are potential motif instances of *Oct4-Sox2*, *Sox2*, *Nanog* and *Klf4* as indicated by the CWMs. **d**, To identify a set of representative motifs from the 33 short motifs discovered for different TFs (information content <30 bit, shown in Supplementary Fig. 3) and remove redundant short motifs, motifs were clustered by similarity using hierarchical clustering. The results were then manually inspected to select clusters that separate known motifs that are distinct (for example *Oct4-Oct4* resembles the known MORE and PORE motifs that bind Oct4 homodimers, which is different from the monomerically bound *Oct4* motif). Among very similar motifs within a cluster, we then selected the most abundant motif that was discovered for the most relevant TF (if known). The 11 representative motifs that we selected are shown on the left. Non-canonical motifs were given a name (*Nanog-alt* for *Nanog alternative*, *Klf4-long* for *longer Klf4*).

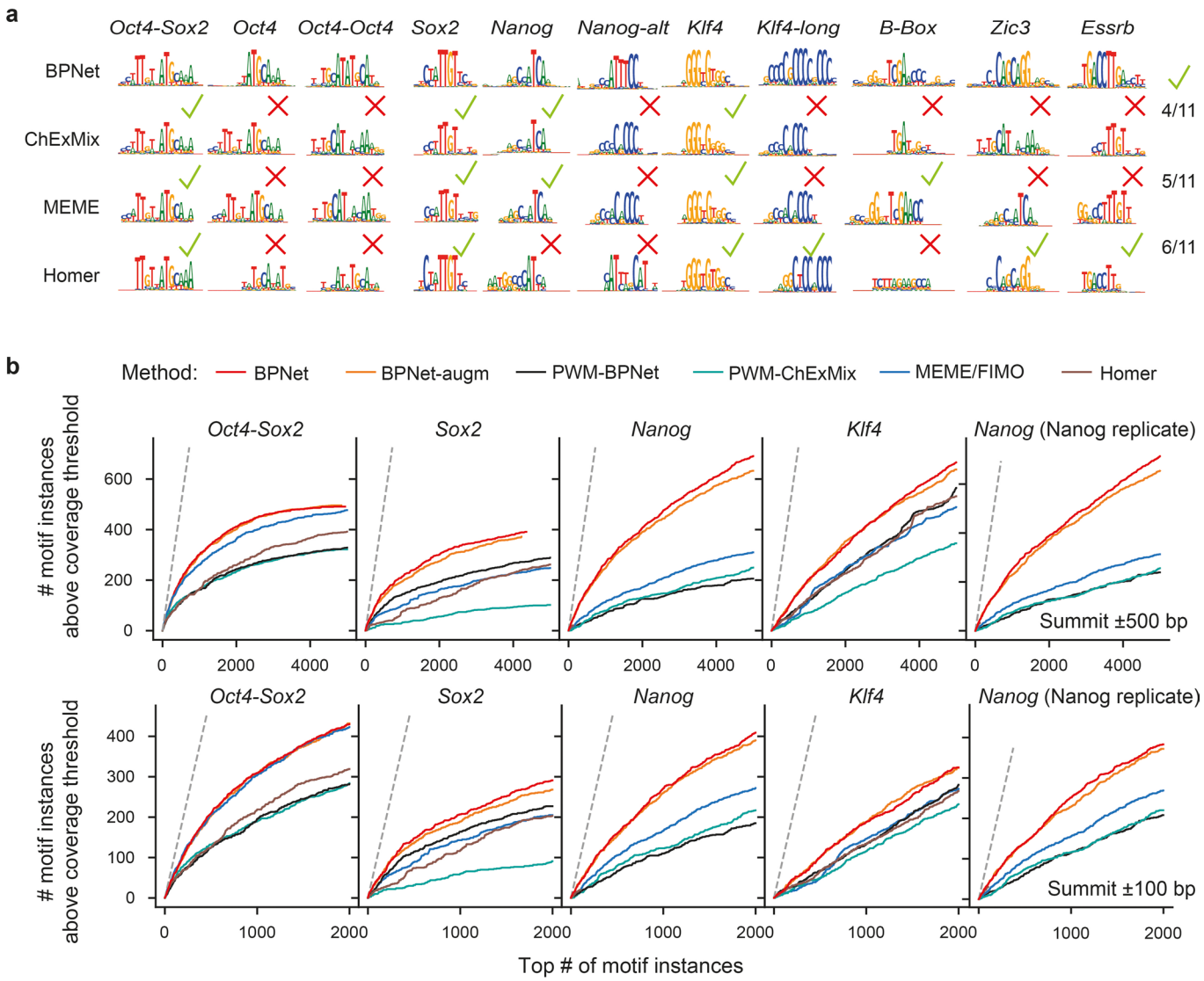

Extended Data Fig. 3 | BPNet and TF-MoDISco outperform traditional methods in motif discovery and the mapping of motif instances. a, Motifs discovered by ChExMix, HOMER and MEME for Oct4, Sox2, Nanog and Klf4 ChIP-nexus peaks that are closest to the 11 primary representative BPNet motifs (top row). Green checkmark denotes whether the discovered motif is similar to the BPNet motif. **b,** Number of motif instances located up to 500 bp (top) or 100 bp (bottom) away from the ChIP-nexus peak summits showing a strong ChIP-nexus footprint. Only motif instances in peaks from held-out test chromosomes (1, 8 and 9) were used for the evaluation. (x-axis) top N motif instances from each of the methods were sorted in descending order of scores (PWM log odds score or CWM contrib score). For BPNet-augm, the center of the genomic region for which the contribution scores were computed was randomly jittered up to 200 bp away from the peak summit. This augmentation prevents BPNet from using the positional information of the peak summit. In the final column (Nanog replicate), the Nanog ChIP-nexus footprint was measured by a separate biological replicate using a different antibody (α-Nanog from Abcam, ab214549), which was not used during training or evaluation.

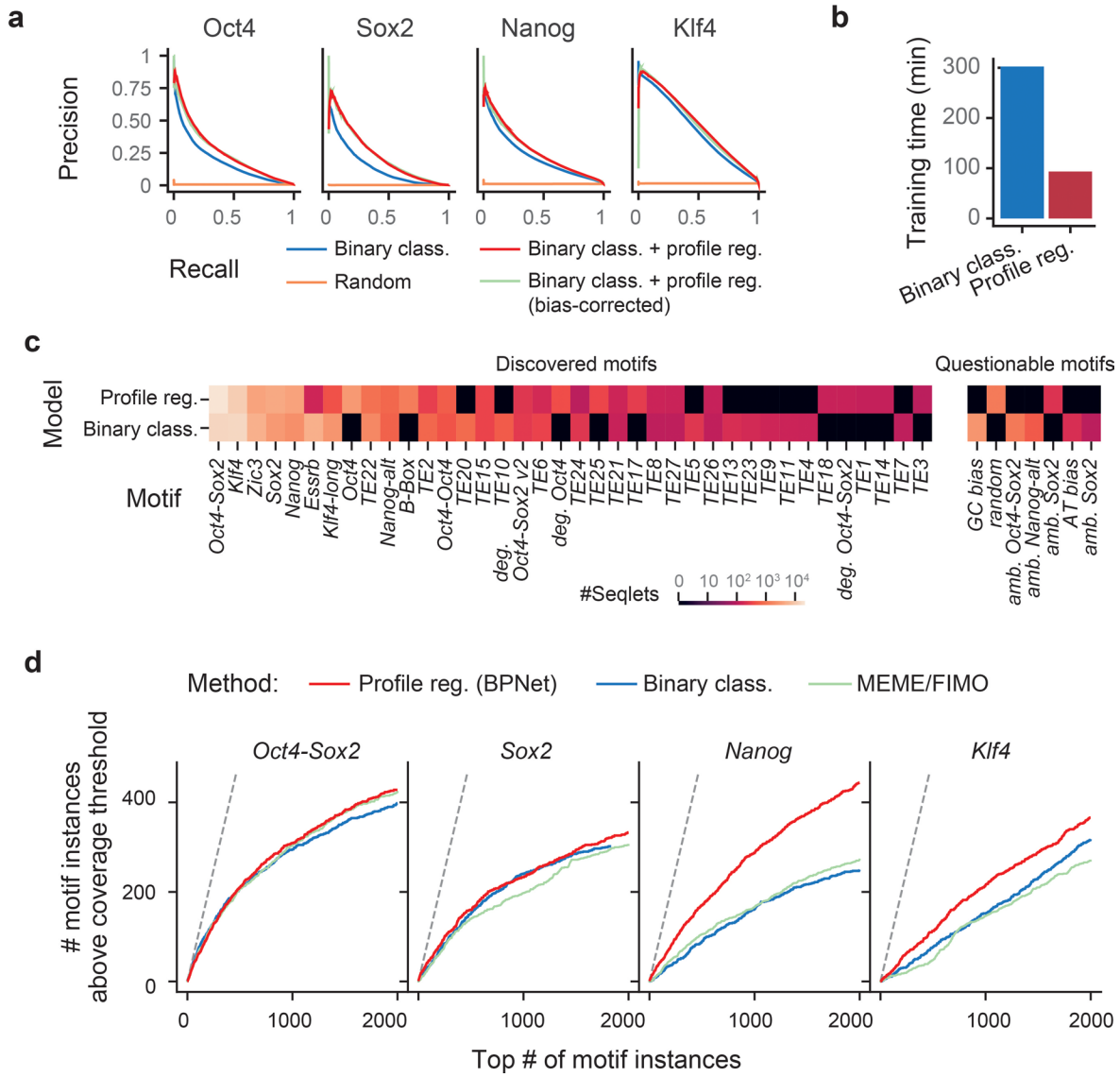

Extended Data Fig. 4 | BPNet training on ChIP-nexus profiles is faster and yields more accurate motif instances than a binary classification model. **a,** Predictive performance as measured by the precision-recall curve of the binary classification models predicting the presence or absence of ChIP-nexus peaks from 1kb DNA sequences evaluated across the held-out (tuning/validation) chromosomes 2, 3 and 4. The model trained to classify the sequences is outperformed when the model is trained to also predict the ChIP-nexus profiles from DNA sequence (without or without profile bias-correction) in addition to classifying them is shown in blue (without or without profile bias-correction) in light blue and with bias-correction in dark blue). **b,** Training time of the binary classification model trained genome-wide and the sequence-to-profile model (BPNet) trained in ChIP-nexus peaks. **c,** Detected motifs by TF-MoDISco using the contribution scores in ChIP-nexus peaks of the sequence-to-profile BPNet (profile reg.) or the binary classification model (binary class). A light color denotes a high number of seqlets for each motif. Motifs not discovered or motifs supported by less than 100 seqlets are shown in black. Questionable motifs are displayed separately on the right. **d,** The number of motif instances (500 bp within ChIP-nexus peak summit) showing a ChIP-nexus footprint (y-axis) within the top N motif instances with highest contribution scores (x-axis) from the held-out (test) chromosomes 1, 8 and 9. A site was considered to show a ChIP-nexus footprint if the number of reads at the position of the aggregate footprint summit (averaged across both strands) is higher than the 90th percentile value of all motif instances detected by the profile regression model for the corresponding TF (that is same as in Extended Data Fig. 3b).

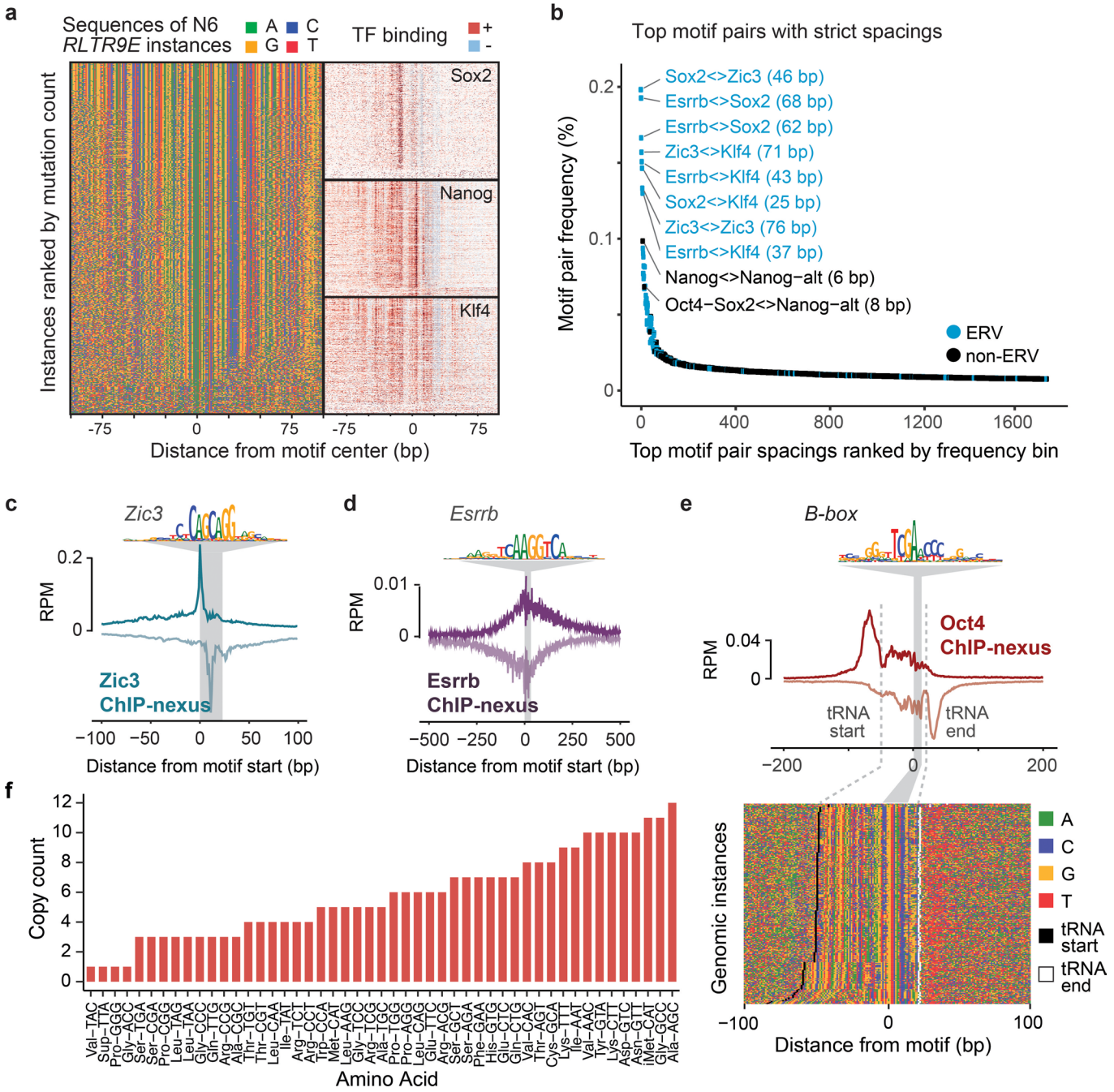

Extended Data Fig. 5 | Strict motif spacings are found on retrotransposons and indirectly bound motifs can be validated. a, To show that TF binding occurs with strict spacings in retrotransposons and that this is likely ancestral, the *RLTR9E N6* motif is shown as an example. Sequences of the individual instances in the genome were sorted by the Kimura distance from the consensus motif, with the most similar sequences on top (which are likely more ancestral). Nanog, Sox2 and Klf4 ChIP-nexus binding footprints are shown in the same order on the right (+ strand reads in red, - strand reads in blue), revealing that the binding site spacing is largely constant across all sequences. **b,** Analysis of the most frequent distances between motif pairs (with >500 co-occurrences, distance measured at the trimmed motifs' centers). The top 1% most frequent distances mapped in 83% to ERVs and were often longer than 20 bp. **c,** To validate the identified *Zic3* motif instances, Zic3 ChIP-nexus experiments were performed. The average signal across the *Zic3* instances reveals a strong Zic3 binding footprint. **d,** A similar validation was performed for the *Esrrb* motif instances, revealing that the Esrrb ChIP-nexus signal is present but more diffuse at the discovered *Esrrb* motif instances. **e,** To better understand the binding of Oct4 to the *B-box*, which is frequently found in tRNA, tRNA-overlapping *B-box* motif instances were reoriented to match the transcriptional direction and sorted by tRNA gene start proximity. This reveals Oct4 binding at tRNA gene start/stop sites. **f,** Amino acid anti-codons and their copy count of the tRNAs that overlapped with the *B-box* motif instances.

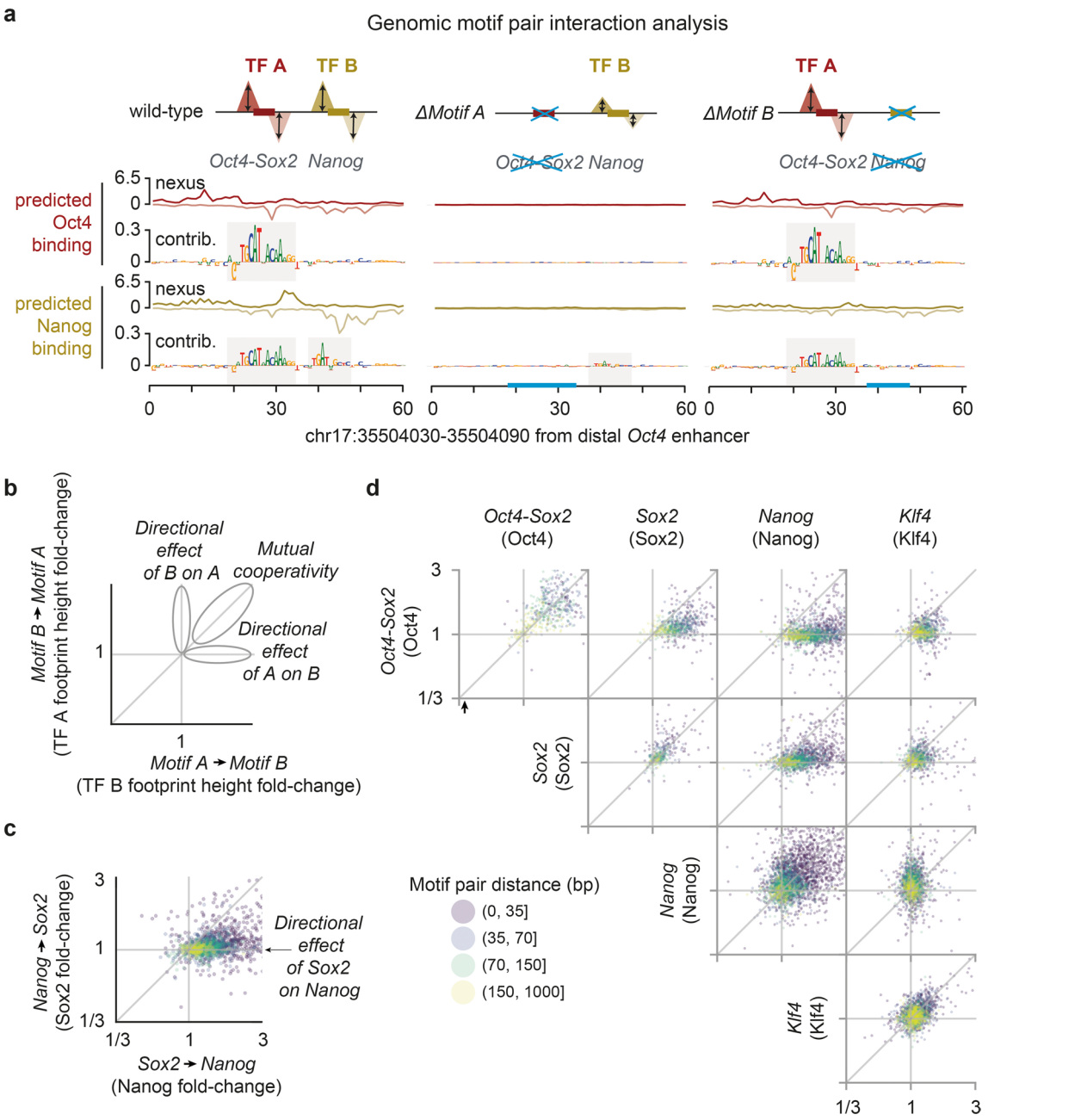

Extended Data Fig. 6 | Additional genomic *in-silico* interaction analyses confirm the directional effects. a, Example genomic *in-silico* mutagenesis analysis at the distal Oct4 enhancer. Predicted ChIP-nexus profiles and the contribution scores greatly decrease at both motifs (*Oct4-Sox2* and *Nanog*) when erasing the *Oct4-Sox2* motif (through random sequence insertion). By contrast, when the Nanog motif is erased (right), the predicted profile and the contribution scores of *Oct4-Sox2* motif remain intact. **b,** Such directional effect of motifs can be quantified by the corrected binding fold change (Supplementary Fig. 10a) for all motif pairs in the genome and visualized as a scatterplot. **c,** Example scatterplot for the interaction between Sox2 and Nanog. Sox2 shows a positive directional effect on Nanog most profound for short motif distances (<35 bp). **d,** Predicted binding fold changes for all motif pairs in genomic sequences.

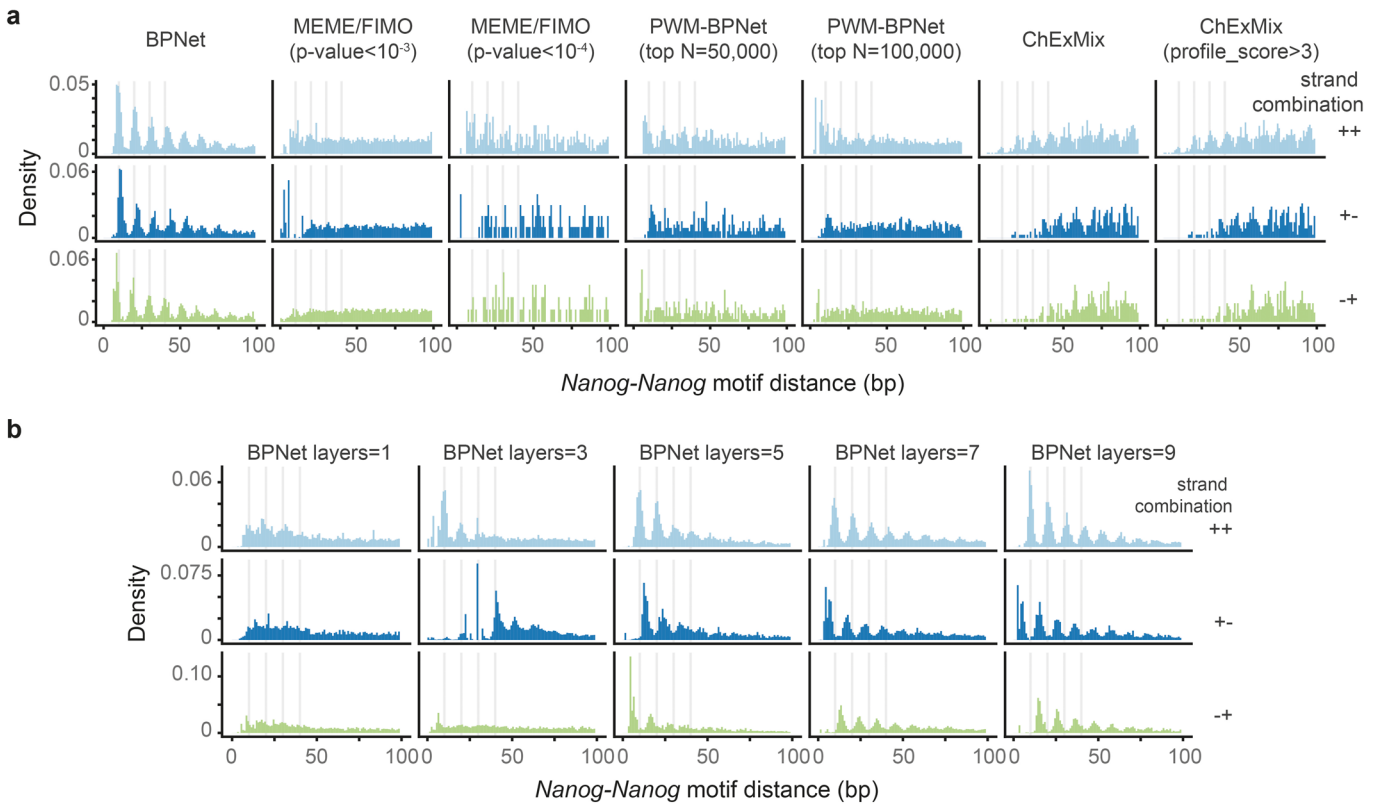

Extended Data Fig. 7 | Helical periodicity of Nanog motifs is not discovered with traditional methods and requires BPNet's large receptive field. **a,** The pairwise spacing of Nanog motif instances located up to 100 bp away from the ChIP-nexus peak summits in all possible strand orientations (rows) for different methods and/or thresholds (columns). Results for all chromosomes are shown. **b,** The pairwise spacing of *Nanog* motif instances when BPNet is trained with different numbers of convolutional layers (Fig. 1g). BPNet with only a single convolutional layer (first column) is unable to capture the 10 bp periodicity due to the limited receptive field similar to PWMs.

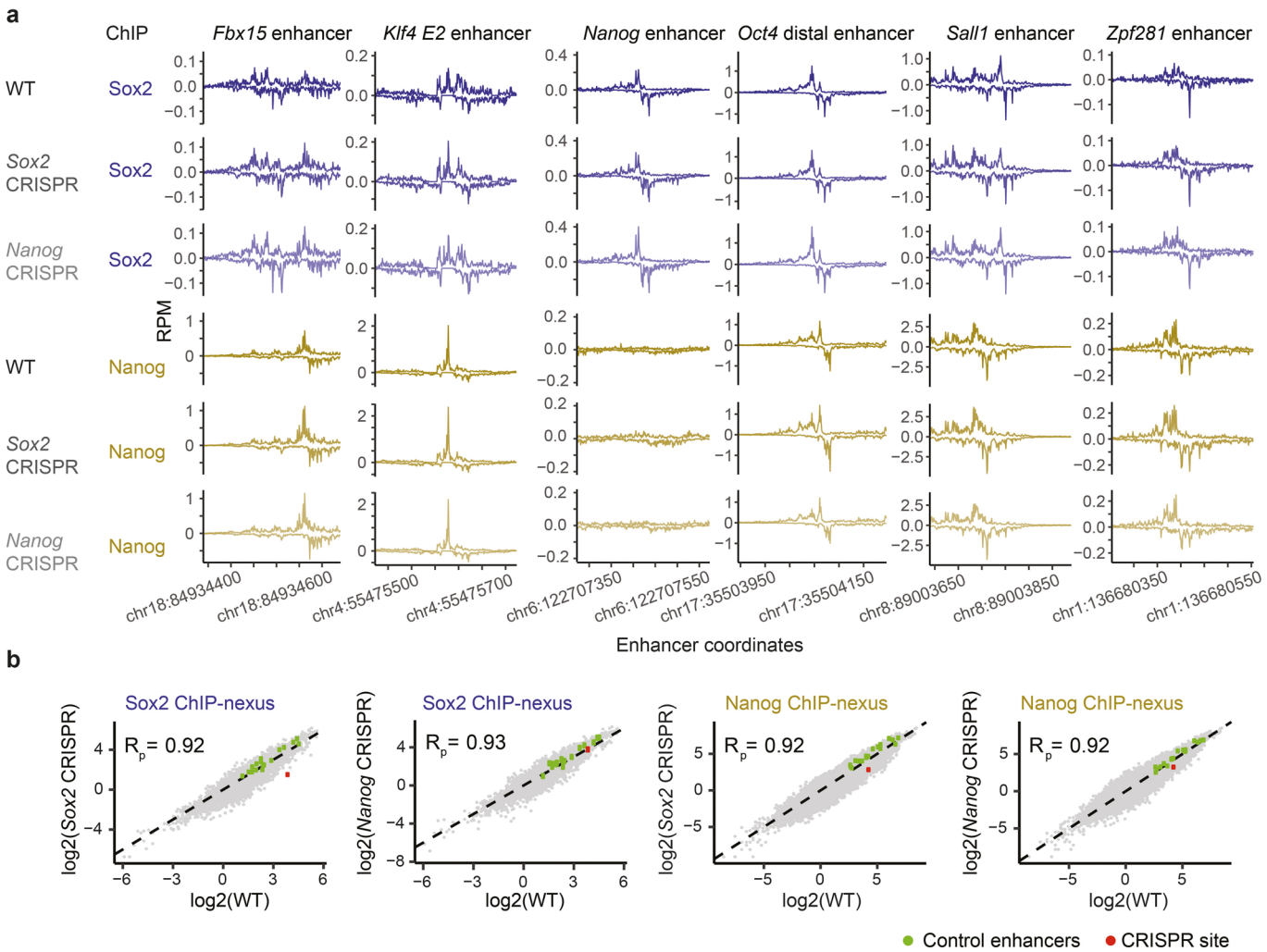

Extended Data Fig. 8 | The ChIP-nexus data on CRISPR-mutated ESCs are highly reproducible. a, Nanog and Sox2 ChIP-nexus profiles normalized to reads per million (RPM) show highly similar profiles and read counts across known enhancer regions for wild-type (Wt) and CRISPR ESCs with either a mutated *Sox2* motif (Sox2 CRISPR) or mutated *Nanog* motif (Nanog CRISPR) at a selected genomic region (chr10: 85,539,626-85,539,777). **b,** Pairwise comparisons of ChIP-nexus RPM counts between Wt and CRISPR ESCs at bound genomic regions (151 bp centered on the respective motif) with Sox2 ChIP-nexus counts on *Sox2* motifs and Nanog ChIP-nexus counts on *Nanog* motifs (motifs based on the original model). The bulk data (gray) are highly correlated and known enhancer regions as shown in Supplementary Fig. 5 (green) are highly reproducible between ESC lines. Note the specific loss of counts in the selected mutated genomic region (red) over wild-type. Pearson correlations (R_p) between groups are shown in the top left of each scatter plot.

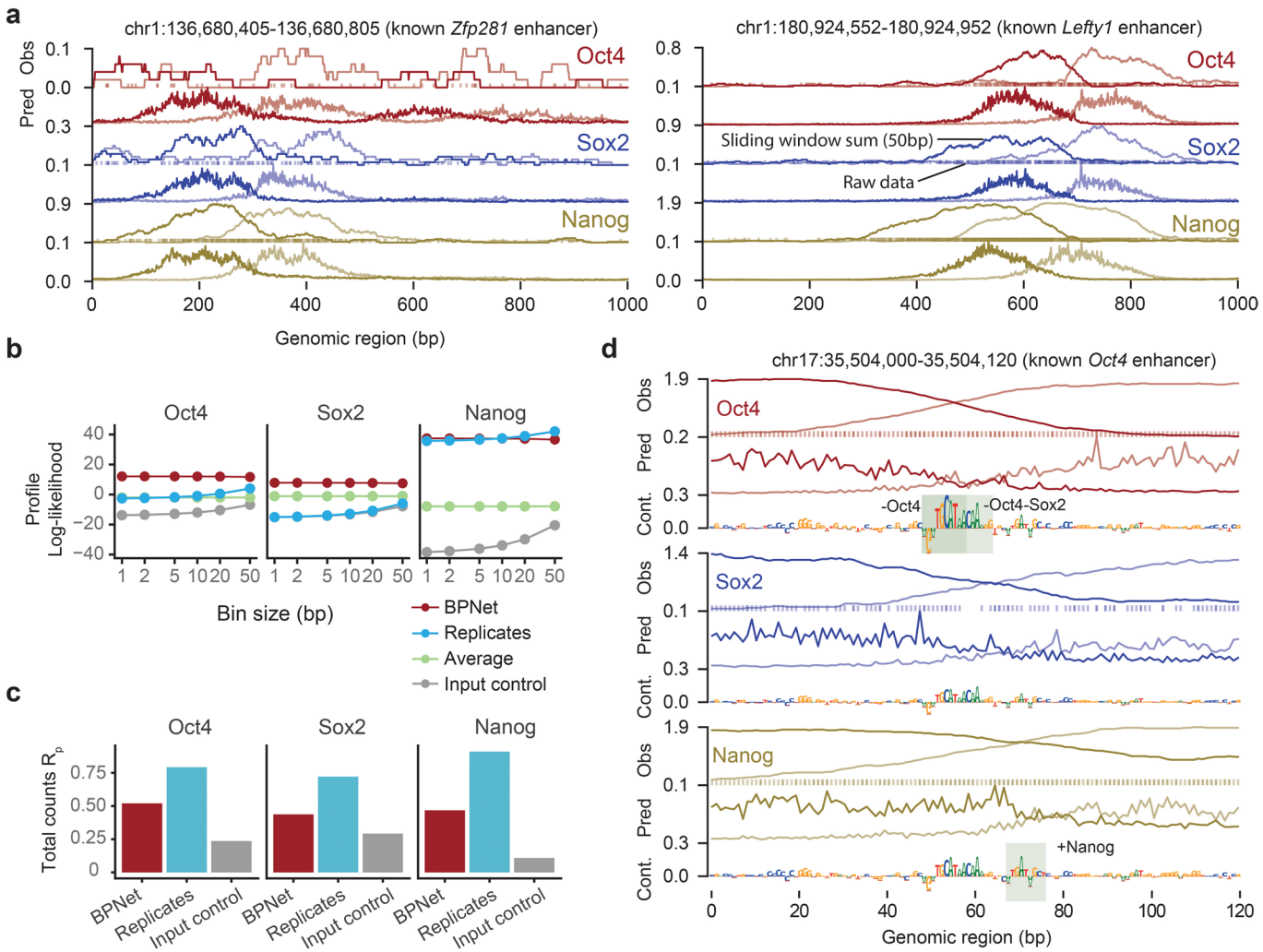

Extended Data Fig. 9 | The base-resolution BPNet model can be trained on ChIP-seq profiles. a, Observed read counts (Obs) and Predicted read counts (Pred) for BPNet trained on ChIP-seq data for the *Zfp281* and *Lefty1* enhancers located on the held-out (test) chromosome 1, with forward strand reads (dark) and reverse strand reads (light). For Obs, a sliding window of 50 bp was used to smooth the raw 5′ end read counts (line); raw counts are shown as points on the bottom at y = 0. **b,** BPNet predicts the ChIP-seq profile shape better than replicates. Multinomial log-likelihood difference compared to the constant model was used to evaluate the profile shape quality at different resolutions (from 1 bp to 10 bp windows) in held-out chromosomes 1, 8 and 9. A log-likelihood of 0 corresponds to the constant model. Multinomial log-likelihood was conditioned on the observed number of total counts as in the training loss. **c,** Total counts in 1 kb regions can be predicted by BPNet (red) at decent accuracy (measured by Pearson correlation with log(1+observed values)). They do not surpass replicate performance (blue), but are well above the Input control (grey). **d,** Obs and Pred as in panel a, as well as contribution scores for the known Oct4 enhancer. Motif instances derived by CWM scanning are highlighted with a green box.

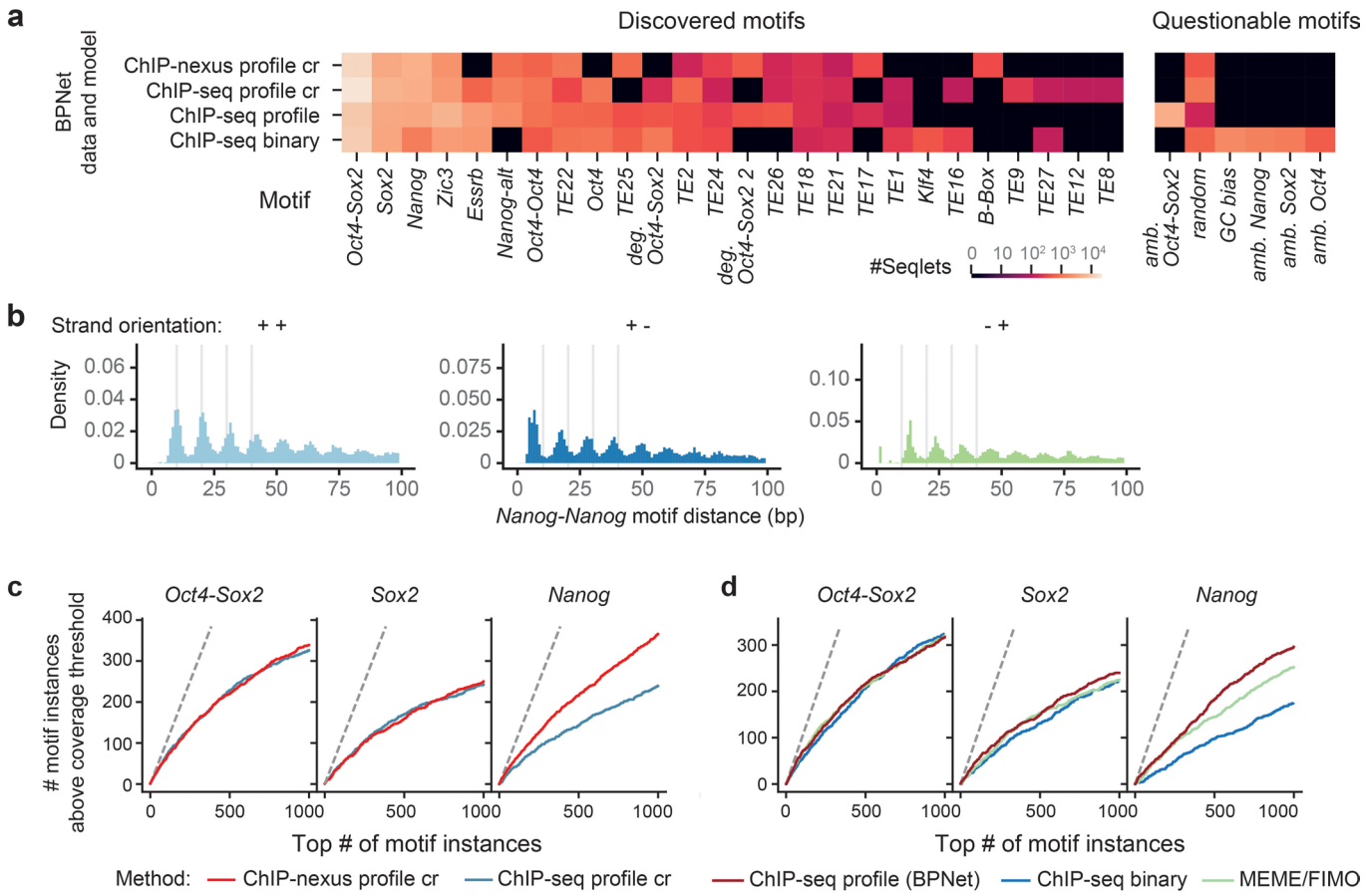

Extended Data Fig. 10 | BPNet trained on ChIP-seq discovers similar motifs and recovers the *Nanog* motif periodicity. a, BPNet applied to ChIP-seq discovers the majority of the motifs identified by BPNet applied to ChIP-nexus data. The models 'ChIP-nexus profile cr' and 'ChIP-seq profile cr' were trained on the union of the ChIP-nexus/seq peaks predicting Oct4, Sox2, and Nanog binding and were interpreted on the intersection of the ChIP-nexus/seq peaks. **b,** The pairwise spacing of *Nanog* motif instances derived from the ChIP-seq profile model in all possible strand orientations shows helical periodicity (similar to Extended Data Fig. 7a). **c**, Motif instance calling with CWM scanning has higher accuracy for BPNet trained on ChIP-nexus data than for BPNet trained on ChIP-seq data (evaluated on the union of the ChIP-nexus/seq peaks, 500 bp around the peak summit using ChIP-nexus footprints as ground truth). **d,** Training a sequence-to-profile model on ChIP-seq data yields more accurate motif instances (500 bp around the ChIP-seq peak summits using ChIP-nexus footprints as ground truth) than training a binary classification model or using a PWM scanning approach using FIMO for motifs derived directly from ChIP-nexus data. See Extended Data Figs. 3b, 4d and Supplementary Note for more details.

nature research

Corresponding author(s): Julia Zeitlinger and Anshul Kundaje

Last updated by author(s): Dec 6, 2020

Reporting Summary

Nature Research wishes to improve the reproducibility of the work that we publish. This form provides structure for consistency and transparency in reporting. For further information on Nature Research policies, see our Editorial Policies and the Editorial Policy Checklist.

Statistics

For all statistical analyses, confirm that the following items are present in the figure legend, table legend, main text, or Methods section.

n/a	Confirmed
☐	☒ The exact sample size (*n*) for each experimental group/condition, given as a discrete number and unit of measurement
☐	☒ A statement on whether measurements were taken from distinct samples or whether the same sample was measured repeatedly
☐	☒ The statistical test(s) used AND whether they are one- or two-sided *Only common tests should be described solely by name; describe more complex techniques in the Methods section.*
☒	☐ A description of all covariates tested
☐	☒ A description of any assumptions or corrections, such as tests of normality and adjustment for multiple comparisons
☐	☒ A full description of the statistical parameters including central tendency (e.g. means) or other basic estimates (e.g. regression coefficient) AND variation (e.g. standard deviation) or associated estimates of uncertainty (e.g. confidence intervals)
☐	☒ For null hypothesis testing, the test statistic (e.g. *F*, *t*, *r*) with confidence intervals, effect sizes, degrees of freedom and *P* value noted *Give P values as exact values whenever suitable.*
☒	☐ For Bayesian analysis, information on the choice of priors and Markov chain Monte Carlo settings
☒	☐ For hierarchical and complex designs, identification of the appropriate level for tests and full reporting of outcomes
☐	☒ Estimates of effect sizes (e.g. Cohen's *d*, Pearson's *r*), indicating how they were calculated

Our web collection on statistics for biologists contains articles on many of the points above.

Software and code

Policy information about availability of computer code

Data collection

ChIP-seq datasets were processed using the ENCODE ChIP-seq pipeline https://github.com/ENCODE-DCC/chip-seq-pipeline2/releases/tag/v1.2.2.

ChIP-nexus datasets were processed using the the code available at: https://github.com/kundajelab/chip-nexus-pipeline. ChIP-nexus reads were trimmed and deduplicated using nimnexus (v0.1.1) available at https://github.com/Avsecz/nimnexus/. ChIP-nexus adapters were trimmed off the reads using cutadapt (v1.8.1). ChIP-nexus reads were aligned using bowtie (v.1.1.12) with the following parameters: --chunkmbs 512 -k 1 -m 1 -v 2 --best --strata. SAMtools (v1.2) was used to flag ChIP-nexus read statistics (SAMtools flagstat) and to filter ChIP-nexus reads (SAMtools view). Aligned ChIP-nexus reads were converted to tagAlign format using bedtools (v2.26). Cross-correlation scores were obtained for each file using phantompeakqualtools (v1.2). UCSC Genome Browser Utilities were used to convert file formats (bedGraphToBigWig v4).

ATAC-seq datasets were processed using the the ENCODE ATAC-seq pipeline (v1.5.3) available at https://github.com/ENCODE-DCC/atac-seq-pipeline. ATAC-seq reads were trimmed using cutadapt (v1.9.1). ATAC-seq reads were aligned using bowtie2 (v2.2.6). SAMtools (v1.2) was used to flag ATAC-seq read statistics (SAMtools flagstat). SAMtools (v1.7) was used to filter ATAC-seq reads (SAMtools view). Picard (v1.126) MarkDuplicates was used to mark duplicated reads. Aligned ATAC-seq reads were converted to tagAlign format using bedtools (v2.26).

MACS2 (v2.1.1.20160309) was used to call ChIP-nexus and ATAC-seq peaks.

Data analysis

Code to reproduce the results is available at https://github.com/kundajelab/bpnet-manuscript (https://doi.org/10.5281/zenodo.4294813).

The BPNet software package is available at https://github.com/kundajelab/bpnet/. All neural network models were implemented and trained in Keras (v2.2.4, TensorFlow backend v1.6) using the Adam optimizer. DeepLIFT was used to derive contribution scores and is available at https://github.com/kundajelab/DeepExplain/ (commit hash: 738c7145e915a7a48f3a4248d088bcc2e1a94614). TF-MoDISco (v0.5.1.1) used DeepLIFT scores to derive motifs.

Discovered motifs were clustered with the Ward variance minimization algorithm and and optimal leaf ordering using scipy (v1.2.1). Discrete Fourier transforms were computed using numpy (v1.16.1). The generalized additive models (GAM) were fit using pygam (v0.7.1) available at https://github.com/dswah/pyGAM. ATAC-seq linear models were trained using scikit-learn (v0.20.1).

ChExMix (v0.3), Homer (v2), and MEME/FIMO (v5.0.2) were used as a benchmarking motif discovery and TF binding event calling method.

All structural renderings used VMD (v1.9.3) with the appropriate STRIDE and SURF binary included in the VMD binary distribution.

MEME Suite's TOMTOM (v5.1.0) was used to identify the TFIIIC B-box.

For manuscripts utilizing custom algorithms or software that are central to the research but not yet described in published literature, software must be made available to editors and reviewers. We strongly encourage code deposition in a community repository (e.g. GitHub). See the Nature Research guidelines for submitting code & software for further information.

Data

Policy information about availability of data

All manuscripts must include a data availability statement. This statement should provide the following information, where applicable:

- Accession codes, unique identifiers, or web links for publicly available datasets
- A list of figures that have associated raw data
- A description of any restrictions on data availability

The raw sequencing data generated in this manuscript are available from GEO under the accession code GSE137193. Data used to train, evaluate, and interpret the BPNet models is available on ZENODO at https://doi.org/10.5281/zenodo.3371164. Trained BPNet models, model predictions and contributions that support the findings of this manuscript from the provided genome browser track, Figure 1, and Figure 2; mapped motif coordinates from the provided genome browser track and summarized in Figure 3; motif pair interaction scores from Figure 4; and motif contribution periodicity from Figure 5 are available on ZENODO at https://doi.org/10.5281/zenodo.3371163. The BPNet model trained on ChIP-nexus data is available on the model repository Kipoi under the name "BPNet-OSKN" (http://kipoi.org/models/BPNet-OSKN/).

ATAC-seq data in mouse ESCs before and after induced depletion of Oct4 and Sox2 that support the findings of this study from Figure 1 and Supplementary Figure 7 have been obtained from GSE134680.

Blacklisted regions used to filter genomic coordinates throughout the analysis are available at https://www.encodeproject.org/files/ENCFF547MET. RepeatMasker mm10 annotations used for classification of genomic regions and analysis in Figure 1, Supplementary Figure 9, Extended Data Figure 2 and Extended Data Figure 5 are available at http://www.repeatmasker.org/genomes/mm10/RepeatMasker-rm405-db20140131/mm10.fa.out.gz. The NMR structure 1O4X used to render Sox2 and Oct1 in Figure 3 is available at https://www.rcsb.org/structure/1o4x. TRANSFAC (v7.0) was used to identify the TFIIIC B-box discussed in Figure 3. The PH0134.1 Pbx PWM used for motif validation in Supplementary Figure 8 and Extended Data Figure 5 was obtained from JASPAR and is available at http://jaspar.genereg.net/api/v1/matrix/PH0134.1.jaspar.
The MA0141.1 Esrrb PWM used for motif validation in Extended Data Figure 5 was obtained from JASPAR and is available at http://jaspar.genereg.net/api/v1/matrix/MA0141.1.jaspar. The tRNA database GtRNAdb (v2.0, release 17.1) annotations and associated tRNAscan-SE scores used to validate the TFIIIC B-box and its association with tRNAs in Extended Data Figure 5 is available at http://gtrnadb.ucsc.edu/GtRNAdb_archives/release17/genomes/eukaryota/Mmusc10/mm10-tRNAs.tar.gz.

Field-specific reporting

Please select the one below that is the best fit for your research. If you are not sure, read the appropriate sections before making your selection.

☒ Life sciences ☐ Behavioural & social sciences ☐ Ecological, evolutionary & environmental sciences

For a reference copy of the document with all sections, see nature.com/documents/nr-reporting-summary-flat.pdf

Life sciences study design

All studies must disclose on these points even when the disclosure is negative.

Sample size	Not applicable. Sample size is not relevant for the machine learning models presented in this work. The models train on 10,000s of genomic regions enriched for TF binding from each genome-wide ChIP-nexus experiment.
Data exclusions	No data was excluded from the analysis.
Replication	All ChIP-nexus and ChIP-seq replicate experiments passed quality control metrics used by ENCODE128 (Supplementary Table 1). The entire pipeline, including the training of BPNet, computing the contribution scores, obtaining motif representations, and analysing motif interactions, was performed in 5-fold cross-validations, which support our claims (Supplementary Information, Supplementary Fig. 4, Supplementary Fig. 11, Supplementary Fig. 12). The CRISPR mutant and wild-type experiments were consistent in profile and counts at control enhancers (Extended Data Fig. 8), and replicate experiments were highly reproducible (Supplementary Figure 14).
Randomization	Not applicable. Randomization is not relevant for this study since it involves a machine learning model trained on genome-wide binding data. Randomization for the purposes of specific statistical or computational analysis is described in the Methods section on a case-by-case basis.
Blinding	Not applicable. Blinding (in the statistical sense) is not relevant for our study that involves a machine learning model trained on genome-wide

Blinding

binding data. The models are validated on held-out chromosomes and using independent experimental methods.

Behavioural & social sciences study design

All studies must disclose on these points even when the disclosure is negative.

Study description	*Briefly describe the study type including whether data are quantitative, qualitative, or mixed-methods (e.g. qualitative cross-sectional, quantitative experimental, mixed-methods case study).*
Research sample	*State the research sample (e.g. Harvard university undergraduates, villagers in rural India) and provide relevant demographic information (e.g. age, sex) and indicate whether the sample is representative. Provide a rationale for the study sample chosen. For studies involving existing datasets, please describe the dataset and source.*
Sampling strategy	*Describe the sampling procedure (e.g. random, snowball, stratified, convenience). Describe the statistical methods that were used to predetermine sample size OR if no sample-size calculation was performed, describe how sample sizes were chosen and provide a rationale for why these sample sizes are sufficient. For qualitative data, please indicate whether data saturation was considered, and what criteria were used to decide that no further sampling was needed.*
Data collection	*Provide details about the data collection procedure, including the instruments or devices used to record the data (e.g. pen and paper, computer, eye tracker, video or audio equipment) whether anyone was present besides the participant(s) and the researcher, and whether the researcher was blind to experimental condition and/or the study hypothesis during data collection.*
Timing	*Indicate the start and stop dates of data collection. If there is a gap between collection periods, state the dates for each sample cohort.*
Data exclusions	*If no data were excluded from the analyses, state so OR if data were excluded, provide the exact number of exclusions and the rationale behind them, indicating whether exclusion criteria were pre-established.*
Non-participation	*State how many participants dropped out/declined participation and the reason(s) given OR provide response rate OR state that no participants dropped out/declined participation.*
Randomization	*If participants were not allocated into experimental groups, state so OR describe how participants were allocated to groups, and if allocation was not random, describe how covariates were controlled.*

Ecological, evolutionary & environmental sciences study design

All studies must disclose on these points even when the disclosure is negative.

Study description	*Briefly describe the study. For quantitative data include treatment factors and interactions, design structure (e.g. factorial, nested, hierarchical), nature and number of experimental units and replicates.*
Research sample	*Describe the research sample (e.g. a group of tagged Passer domesticus, all Stenocereus thurberi within Organ Pipe Cactus National Monument), and provide a rationale for the sample choice. When relevant, describe the organism taxa, source, sex, age range and any manipulations. State what population the sample is meant to represent when applicable. For studies involving existing datasets, describe the data and its source.*
Sampling strategy	*Note the sampling procedure. Describe the statistical methods that were used to predetermine sample size OR if no sample-size calculation was performed, describe how sample sizes were chosen and provide a rationale for why these sample sizes are sufficient.*
Data collection	*Describe the data collection procedure, including who recorded the data and how.*
Timing and spatial scale	*Indicate the start and stop dates of data collection, noting the frequency and periodicity of sampling and providing a rationale for these choices. If there is a gap between collection periods, state the dates for each sample cohort. Specify the spatial scale from which the data are taken*
Data exclusions	*If no data were excluded from the analyses, state so OR if data were excluded, describe the exclusions and the rationale behind them, indicating whether exclusion criteria were pre-established.*
Reproducibility	*Describe the measures taken to verify the reproducibility of experimental findings. For each experiment, note whether any attempts to repeat the experiment failed OR state that all attempts to repeat the experiment were successful.*
Randomization	*Describe how samples/organisms/participants were allocated into groups. If allocation was not random, describe how covariates were controlled. If this is not relevant to your study, explain why.*
Blinding	*Describe the extent of blinding used during data acquisition and analysis. If blinding was not possible, describe why OR explain why blinding was not relevant to your study.*

Did the study involve field work? ☐ Yes ☐ No

Field work, collection and transport

Field conditions	*Describe the study conditions for field work, providing relevant parameters (e.g. temperature, rainfall).*
Location	*State the location of the sampling or experiment, providing relevant parameters (e.g. latitude and longitude, elevation, water depth).*
Access & import/export	*Describe the efforts you have made to access habitats and to collect and import/export your samples in a responsible manner and in compliance with local, national and international laws, noting any permits that were obtained (give the name of the issuing authority, the date of issue, and any identifying information).*
Disturbance	*Describe any disturbance caused by the study and how it was minimized.*

Reporting for specific materials, systems and methods

We require information from authors about some types of materials, experimental systems and methods used in many studies. Here, indicate whether each material, system or method listed is relevant to your study. If you are not sure if a list item applies to your research, read the appropriate section before selecting a response.

Materials & experimental systems

n/a	Involved in the study
☐	☒ Antibodies
☐	☒ Eukaryotic cell lines
☒	☐ Palaeontology and archaeology
☒	☐ Animals and other organisms
☒	☐ Human research participants
☒	☐ Clinical data
☒	☐ Dual use research of concern

Methods

n/a	Involved in the study
☐	☒ ChIP-seq
☒	☐ Flow cytometry
☒	☐ MRI-based neuroimaging

Antibodies

Antibodies used	α-Oct3/4 (Santa Cruz, sc-8628), α-Sox2 (Santa Cruz, sc-17320), α-Sox2 (Active Motif, 39843), α-Nanog (Santa Cruz, sc-30328), α-Nanog (Abcam, ab214549), α-Klf4 (R&D Systems, AF3158), α-Klf4 (Abcam, ab106629), α-Esrrb (Abcam, ab19331), α-Pbx 1/2/3 (Santa Cruz, sc-888), and α-Zic3 (Abcam, ab222124). 5 µg of each antibody was used for per ChIP experiment.
Validation	The antibodies used are commercially validated antibodies. We additionally validated for Sox2 and Nanog by performing ChIP-nexus experiments for the same factor using different antibodies. For the initial wild-type Sox2 ChIP-nexus experiments, we used two different antibodies with IDR rescue ratio of <2, confirming the dataset consistency. For the wild-type and CRISPR Nanog ChIP-nexus experiments, we also used two different antibodies (sc-30328 and ab-214549). In Extended Data Figure 3, we validate that the discovered motifs were consistent between the wild-type and CRISPR Nanog ChIP-nexus experiments.

Eukaryotic cell lines

Policy information about cell lines

Cell line source(s)	Mouse R1 embryonic stem cells (ATCC ® SCRC-1011 ™)
Authentication	The cell line was not authenticated.
Mycoplasma contamination	The cells were tested negative for mycoplasma by the Stowers core facility.
Commonly misidentified lines (See ICLAC register)	No commonly misidentified cell lines were used in the study as per the ICLAC Register v10.

Palaeontology and Archaeology

Specimen provenance	*Provide provenance information for specimens and describe permits that were obtained for the work (including the name of the issuing authority, the date of issue, and any identifying information).*
Specimen deposition	*Indicate where the specimens have been deposited to permit free access by other researchers.*
Dating methods	*If new dates are provided, describe how they were obtained (e.g. collection, storage, sample pretreatment and measurement), where they were obtained (i.e. lab name), the calibration program and the protocol for quality assurance OR state that no new dates are provided.*

☐ Tick this box to confirm that the raw and calibrated dates are available in the paper or in Supplementary Information.

Ethics oversight	*Identify the organization(s) that approved or provided guidance on the study protocol, OR state that no ethical approval or guidance was required and explain why not.*

Note that full information on the approval of the study protocol must also be provided in the manuscript.

Animals and other organisms

Policy information about studies involving animals; ARRIVE guidelines recommended for reporting animal research

Laboratory animals	*For laboratory animals, report species, strain, sex and age OR state that the study did not involve laboratory animals.*
Wild animals	*Provide details on animals observed in or captured in the field; report species, sex and age where possible. Describe how animals were caught and transported and what happened to captive animals after the study (if killed, explain why and describe method; if released, say where and when) OR state that the study did not involve wild animals.*
Field-collected samples	*For laboratory work with field-collected samples, describe all relevant parameters such as housing, maintenance, temperature, photoperiod and end-of-experiment protocol OR state that the study did not involve samples collected from the field.*
Ethics oversight	*Identify the organization(s) that approved or provided guidance on the study protocol, OR state that no ethical approval or guidance was required and explain why not.*

Note that full information on the approval of the study protocol must also be provided in the manuscript.

Human research participants

Policy information about studies involving human research participants

Population characteristics	*Describe the covariate-relevant population characteristics of the human research participants (e.g. age, gender, genotypic information, past and current diagnosis and treatment categories). If you filled out the behavioural & social sciences study design questions and have nothing to add here, write "See above."*
Recruitment	*Describe how participants were recruited. Outline any potential self-selection bias or other biases that may be present and how these are likely to impact results.*
Ethics oversight	*Identify the organization(s) that approved the study protocol.*

Note that full information on the approval of the study protocol must also be provided in the manuscript.

Clinical data

Policy information about clinical studies

All manuscripts should comply with the ICMJE guidelines for publication of clinical research and a completed CONSORT checklist must be included with all submissions.

Clinical trial registration	*Provide the trial registration number from ClinicalTrials.gov or an equivalent agency.*
Study protocol	*Note where the full trial protocol can be accessed OR if not available, explain why.*
Data collection	*Describe the settings and locales of data collection, noting the time periods of recruitment and data collection.*
Outcomes	*Describe how you pre-defined primary and secondary outcome measures and how you assessed these measures.*

Dual use research of concern

Policy information about dual use research of concern

Hazards

Could the accidental, deliberate or reckless misuse of agents or technologies generated in the work, or the application of information presented in the manuscript, pose a threat to:

No	Yes	
☐	☐	Public health
☐	☐	National security
☐	☐	Crops and/or livestock
☐	☐	Ecosystems
☐	☐	Any other significant area

Experiments of concern

Does the work involve any of these experiments of concern:

No	Yes	
☐	☐	Demonstrate how to render a vaccine ineffective
☐	☐	Confer resistance to therapeutically useful antibiotics or antiviral agents
☐	☐	Enhance the virulence of a pathogen or render a nonpathogen virulent
☐	☐	Increase transmissibility of a pathogen
☐	☐	Alter the host range of a pathogen
☐	☐	Enable evasion of diagnostic/detection modalities
☐	☐	Enable the weaponization of a biological agent or toxin
☐	☐	Any other potentially harmful combination of experiments and agents

ChIP-seq

Data deposition

☒ Confirm that both raw and final processed data have been deposited in a public database such as GEO.

☒ Confirm that you have deposited or provided access to graph files (e.g. BED files) for the called peaks.

Data access links *May remain private before publication.*	The raw sequencing data are available from GEO under the accession number GSE137193 with the token wfolwmugzhurvqr. Processed data are available here: https://doi.org/10.5281/zenodo.3371164.
Files in database submission	Oct4-ChIP-nexus Sox2-ChIP-nexus Nanog-ChIP-nexus Klf4-ChIP-nexus PAtCh-Cap Essrb-ChIP-nexus Pbx-ChIP-nexus Zic3-ChIP-nexus Oct4-ChIP-seq Sox2-ChIP-seq Nanog-ChIP-seq Input-control-ChIP-seq CRISPR.wt.Nanog CRISPR.wt.Sox2 CRISPR.mutant.sox2crispr1.Nanog CRISPR.mutant.sox2crispr1.Sox2 CRISPR.mutant.nanogcrispr1.Nanog CRISPR.mutant.nanogcrispr1.Sox2
Genome browser session (e.g. UCSC)	https://genome.ucsc.edu/s/mlweilert/mesc_OSKN_tracks

Methodology

Replicates	At least two biological replicates were performed for each factor.
Sequencing depth	The total read coverage for each factor is at least 100 million reads per transcription factor.
Antibodies	α-Oct3/4 (Santa Cruz, sc-8628), α-Sox2 (Santa Cruz, sc-17320), α-Sox2 (Active Motif, 39843), α-Nanog (Santa Cruz, sc-30328), α-Klf4 (R&D Systems, AF3158), α-Klf4 (Abcam, ab106629), α-Esrrb (Abcam, ab19331), α-Pbx 1/2/3 (Santa Cruz, sc-888), and α-Zic3 (Abcam, ab222124). 5 µg of each antibody was used for per ChIP experiment.
Peak calling parameters	Peaks were called using MACS2 (v2.1.1.20160309) by extending 5'-ends of reads on each strand using a 150 bp window (±75 bp) and then computing coverage of extended reads across both strands (shift=-75, extsize=150). For each TF, peak calling was performed on filtered, aligned reads from each replicate using a relaxed p-value threshold of 0.1 and retaining the top 300,000 peaks as described in 130. Relaxed peak calls were also similarly obtained from pseudo-replicates, which were obtained by pooling filtered, aligned reads from all replicates for a TF and randomly splitting the pooled reads into two balanced pseudo-replicates. We used the Irreproducible Discovery Rate (IDR) framework to obtain reproducible peaks across the true-replicates and pseudo-replicates 132. The larger of these two sets of IDR peaks (in terms of number of peaks) was defined as the "IDR optimal set" of peaks for each TF. Peaks overlaping the blacklisted regions listed in http://mitra.stanford.edu/kundaje/akundaje/release/blacklists/mm10-mouse/mm10.blacklist.bed.gz were excluded.
Data quality	We computed several quality control metrics to evaluate enrichment and reproducibility of our ChIP-nexus datasets based on the ENCODE TF ChIP-seq pipeline and quality control standards 130 (Supplemental table 1). We computed the fraction of reads in IDR optimal peaks (FRiP) as an estimate of enrichment. All our samples had uniformly high FRiP scores. We also computed the "rescue

ratio" i.e. the ratio of the number of IDR optimal peaks from pseudo-replicates to the number of IDR optimal peaks from the true replicates, as an estimate of reproducibility. For all four TFs, ChIP-nexus samples had Rescue Ratios < 2 and had tens of thousands of reproducible peaks indicating high reproducibility of the datasets. The IDR optimal peaks from ChIP-nexus data also showed strong overlap with IDR optimal peaks from corresponding ChIP-seq data targeting the same TFs.

Software

The nim-nexus code is available at https://github.com/Avsecz/nimnexus/. The ChIP-nexus pipeline performing the described steps (e.g. turning the raw reads in the FASTQ format to BigWig coverage tracks and the called peaks) is available at https://github.com/kundajelab/chip-nexus-pipeline. A detailed pipeline specification is available at https://docs.google.com/document/d/1h9lZ0GyVWd02RCmtaFWSaSFzrcNHoH_OgyPHMpU7b04.

Flow Cytometry

Plots

Confirm that:

☐ The axis labels state the marker and fluorochrome used (e.g. CD4-FITC).

☐ The axis scales are clearly visible. Include numbers along axes only for bottom left plot of group (a 'group' is an analysis of identical markers).

☐ All plots are contour plots with outliers or pseudocolor plots.

☐ A numerical value for number of cells or percentage (with statistics) is provided.

Methodology

Sample preparation

Describe the sample preparation, detailing the biological source of the cells and any tissue processing steps used.

Instrument

Identify the instrument used for data collection, specifying make and model number.

Software

Describe the software used to collect and analyze the flow cytometry data. For custom code that has been deposited into a community repository, provide accession details.

Cell population abundance

Describe the abundance of the relevant cell populations within post-sort fractions, providing details on the purity of the samples and how it was determined.

Gating strategy

Describe the gating strategy used for all relevant experiments, specifying the preliminary FSC/SSC gates of the starting cell population, indicating where boundaries between "positive" and "negative" staining cell populations are defined.

☐ Tick this box to confirm that a figure exemplifying the gating strategy is provided in the Supplementary Information.

Magnetic resonance imaging

Experimental design

Design type

Indicate task or resting state; event-related or block design.

Design specifications

Specify the number of blocks, trials or experimental units per session and/or subject, and specify the length of each trial or block (if trials are blocked) and interval between trials.

Behavioral performance measures

State number and/or type of variables recorded (e.g. correct button press, response time) and what statistics were used to establish that the subjects were performing the task as expected (e.g. mean, range, and/or standard deviation across subjects).

Acquisition

Imaging type(s)

Specify: functional, structural, diffusion, perfusion.

Field strength

Specify in Tesla

Sequence & imaging parameters

Specify the pulse sequence type (gradient echo, spin echo, etc.), imaging type (EPI, spiral, etc.), field of view, matrix size, slice thickness, orientation and TE/TR/flip angle.

Area of acquisition

State whether a whole brain scan was used OR define the area of acquisition, describing how the region was determined.

Diffusion MRI ☐ Used ☐ Not used

Preprocessing

Preprocessing software

Provide detail on software version and revision number and on specific parameters (model/functions, brain extraction, segmentation, smoothing kernel size, etc.).

Normalization

If data were normalized/standardized, describe the approach(es): specify linear or non-linear and define image types used for transformation OR indicate that data were not normalized and explain rationale for lack of normalization.

Normalization template

Describe the template used for normalization/transformation, specifying subject space or group standardized space (e.g. original Talairach, MNI305, ICBM152) OR indicate that the data were not normalized.

Noise and artifact removal

Describe your procedure(s) for artifact and structured noise removal, specifying motion parameters, tissue signals and physiological signals (heart rate, respiration).

Volume censoring

Define your software and/or method and criteria for volume censoring, and state the extent of such censoring.

Statistical modeling & inference

Model type and settings

Specify type (mass univariate, multivariate, RSA, predictive, etc.) and describe essential details of the model at the first and second levels (e.g. fixed, random or mixed effects; drift or auto-correlation).

Effect(s) tested

Define precise effect in terms of the task or stimulus conditions instead of psychological concepts and indicate whether ANOVA or factorial designs were used.

Specify type of analysis: ☐ Whole brain ☐ ROI-based ☐ Both

Statistic type for inference
(See Eklund et al. 2016)

Specify voxel-wise or cluster-wise and report all relevant parameters for cluster-wise methods.

Correction

Describe the type of correction and how it is obtained for multiple comparisons (e.g. FWE, FDR, permutation or Monte Carlo).

Models & analysis

n/a	Involved in the study
☐	☐ Functional and/or effective connectivity
☐	☐ Graph analysis
☐	☐ Multivariate modeling or predictive analysis

Functional and/or effective connectivity

Report the measures of dependence used and the model details (e.g. Pearson correlation, partial correlation, mutual information).

Graph analysis

Report the dependent variable and connectivity measure, specifying weighted graph or binarized graph, subject- or group-level, and the global and/or node summaries used (e.g. clustering coefficient, efficiency, etc.).

Multivariate modeling and predictive analysis

Specify independent variables, features extraction and dimension reduction, model, training and evaluation metrics.